

Imaging of Seawater Motion Signatures Using Remote Sensors

Chapter Outline

5.1. Aerial Photography in the Visible and Infrared Bands	140	5.4. Active Microwave Radar Imaging Technologies	154
5.2. Remote Detection by Radiometers	141	5.4.1. Active Microwave Imaging by the RAR Systems	155
5.2.1. Passive Radiometry in the Visible-Wavelength Band	142	5.4.2. Active Microwave Imaging by SAR Systems	158
5.2.2. Active Radiometry in the Visible-Wavelength Band	145	5.4.2.1. Synthesis of Long Antenna from Small Antenna	159
5.2.3. Passive Radiometry in the Thermal Infrared Band	146	5.4.2.2. Enhancement of Azimuth Resolution	160
5.2.3.1. Detectors	147	5.4.2.3. Sources of Errors	163
5.2.3.2. Atmospheric Effects and Correction	148	5.4.2.4. Interferometric SAR (InSAR) System	165
5.2.3.3. SST Imaging	148	5.5. Advances in the Development of SAR Technology	166
5.2.4. Microwave Radiometers	149	5.5.1. Interpretation of Image Data	167
5.2.4.1. Principle of Passive Microwave Radiometry	150	5.6. Detection of Seawater Circulation Features Using RAR and SAR	168
5.2.4.2. Passive Microwave Radiometer Instrumentation	150	5.7. Measurement of Sea Surface Currents Using Imaging of Ice Floes	170
5.2.4.3. Scanning Multichannel Radiometers	151	References	171
5.3. Active Microwave Radar Imaging of Sea Surface Current Signatures	153	Bibliography	174

The human brain is especially good at pattern recognition; therefore, an advantage of obtaining imagery is that it helps us achieve clear understanding of several visually observable phenomena (e.g., signatures of various kinds of seawater motions) through images of them. Images are obtained through a wide variety of remote sensing technologies (i.e., technologies for making measurements from a distance without having direct physical contact). Images of seawater motion signatures are constructed based on the characteristics of electromagnetic radiations that are reflected or scattered from or emitted by the sea surface. Modern remote sensing devices include passive and active systems; they employ different bands in the visible, infrared, microwave, very high-frequency (VHF), ultra high-frequency (UHF), and high-frequency (HF) regions in the electromagnetic spectrum.

Fortunately, the Earth's atmosphere is almost completely transparent to all these radiation bands when cloud-free and nearly so to radio waves, even when clouds are present. This

is one of the reasons for the wide application of space technologies to remotely sense several of the sea surface signatures, such as those pertaining to ocean currents and their manifestations. A remarkable feature of remote sensing technologies is their ability to obtain synoptic and repetitive coverage of large and inaccessible areas. Technical and economic feasibilities of remote sensing technologies for regional and global monitoring of the changing oceanic environmental conditions have been demonstrated through several experimental, semi-operational, and operational studies the world over. Apart from academic interest, remote sensing through space-based systems offers unique possibilities for systematic and timely acquisition of information on sea surface features, with short turnaround times for use by environmental and fisheries scientists as well as coast guard and tactical personnel. Ocean surveillance by remote sensors has already grown to a very useful operational level.

Sensors that detect natural radiation, either emitted or reflected from the sea surface, are known as *passive*

sensors. In the oceanographic context, sensors that produce and then transmit their own electromagnetic radiation onto the sea surface and subsequently detect the return radiations are called *active sensors*. Sensors can be either *imaging* types or *nonimaging* types. The focus of this chapter is the imaging types of sensor for remotely detecting the sea surface manifestations of various types of seawater motions. Satellite remote sensing observations (sea surface temperature, color, and roughness) are utilized to characterize the circulation processes and patterns in the upper layer of the oceans.

5.1. AERIAL PHOTOGRAPHY IN THE VISIBLE AND INFRARED BANDS

Sea surface roughness and color contrasts are the two major types of signatures that are often utilized in the detection of sea surface current patterns with the aid of aerial photography in the visible and infrared bands. These contrasts provide visual indication of the surface manifestations of seawater motions. Sea surface roughness changes from the combined effect of varying wind stress in the marine atmospheric boundary layer, or MABL (induced by the sea surface temperature front), and surface current convergence and divergence (induced by the meandering current). In particular, the changes in the stratification of the MABL and subsequent wind stress changes produce a step-like drop of the sea surface roughness at the downwind side of the front (Johannessen et al., 2005). The color signatures are usually those of chlorophyll, algae, and suspended-sediment plumes. Whereas chlorophyll and algal blooms are often indicative of upwelling motions, the suspended sediment plumes often arise from river discharges into the bluer, clearer seawater. The plume of turbid brown water is easily detectable in the visible wavelength photographs. In the initial years of oceanographic studies, time-lapsed aerial photography from overhead was employed to obtain information on water motion from such images.

The turbid brown water often assumes a lobate or relatively smooth convex front that maintains its integrity as it moves in response to the sea surface currents. The size and history of movement of the plumes can be investigated from a series of time-lapse aerial photographs. The photographic gray tone and, in the case of colored imagery, the color tone are very important in the interpretation of sea surface water circulation features. Relative ages of multiple plume fronts representing discrete water bodies in gulfs could also be determined from aerial photographs by examining the overlapping relations of plumes with differing sediment concentrations; the older, less turbid plumes probably have lower sediment concentrations. This means that aerial photography can provide a synoptic view of discrete water masses that can be differentiated by suspended sediment

load. If clearer water is absent, the prevailing circulation pattern can be deduced from density patterns of turbid water. There were instances in which small-scale eddies could be detected using photo-density analysis of aerial photographs of suspended-sediment plumes (Verstappen, 1977). For photographic investigation of plumes, the aircraft is generally flown at altitudes of 10,000 feet or less.

Aerial photography has been used as an effective tool for identifying water-motion patterns in gulfs, estuaries, and frontal regions. Another remote sensing technology effectively used for detection of sea surface circulation patterns is the sensing of sea surface roughness. Oceanic regions that are dominated by intense currents are often marked by a roughness contrast of the sea surface compared to those of the adjacent regions with no significant currents. For example, mariners knew for centuries that the Gulf Stream often exhibited atypical waves. When waves oppose currents, a much rougher surface is produced. When currents are present away from shallow depths, the initial waves are transformed into higher-amplitude waves with shorter wavelengths and more whitecaps. Although the wave period remains essentially unchanged, the roughness (root-mean-square wave slope) is greatly increased, i.e., the wavelength decreases and amplitude increases. The waves ultimately break when their steepness increases to a point where they become unstable.

The amplitude and maximum slope of a progressive wave just starting to break lie near the theoretical values of the wave's height-to-length ratio of 0.14 and 30° , respectively. In some instances, wave-current interaction, particularly wave blocking, is thought to be the mechanism responsible for increased roughness of the sea surface. Witting (1984) observed that wave blocking, which can occur when a wave field propagates into a spatially increasing current, is especially effective in altering the properties of the wave field. Wave blocking by a current, u , occurs when the component of the group velocity of the wave aligned with the current matches the magnitude of u . Wave blocking, breaking, and refraction may occur even when the waves do not advance directly into the current. Similarly, if a train of surface gravity waves runs in the direction of a surface current, their absolute progression is enhanced, with a resulting decrease in wave amplitude. The wave-current interaction resulting in wave-amplitude modification becomes more noticeable for short waves because their phase velocity is comparable to the prevailing sea surface currents. Swell waves for which the phase velocities are appreciably larger than the prevailing surface circulation velocities do not contribute to surface roughness contrasts arising from wave-current interactions.

If there is a convergence or divergence of the current, the roughness "contrast" along the line of convergence or divergence, arising from wave amplitude contrast, will be very predominant compared to that in the surrounding

regions. It is known that there is often a surface convergence associated with fronts due to secondary circulation in the vertical plane at right angles to the geostrophic flow of the front.

As a result of wave-current interaction, the water flow path will be associated with a sharp contrast in the appearance of the surface wave pattern. These contrasts can be seen in the sea surface images. Therefore these images permit identification of the sea surface current circulation path. This is one of the principles behind remote detection of sea surface circulation using visible-wavelength photography.

A classical example of a current circulation pattern that can be clearly seen in visible-wavelength photography is the surf zone circulation cells consisting of longshore and rip currents. Inman et al. (1971) provided an excellent aerial photograph of the surf zone current showing an evenly spaced jet-like rip current carrying material from the surf zone and producing vortex pairs. The spacing between the rip currents determines the longshore dimensions of the nearshore circulation cell. In the wave zone, sea surface currents and waves are each influenced by the other in different ways. For example, Strong et al. (2000, 2003) examined the modifications undergone by waves propagating through regions with a significant mean current.

An important photographically detectable circulation feature is isolated vortices in the flow field. Such vortices are often produced by the shear between an intense current and its adjacent stagnant water mass. It is known that the shear region between the Kuroshio current in the East China Sea and the Pacific coast is populated with several isolated vortices of various scales. The motions of these vortices can be surveyed from time-series aerial photographs. The large roughness signature of these vortices in contrast to the surrounding water masses makes them clearly visible in the aerial photographs. Very fast tidal currents in straits are also associated with isolated vortices. For example, the intense tidal current (approximately 10 knots) in the Naruto Strait in Japan has many vortices for which the diameter usually exceeds 20 meters and water surface depression exceeds 2 meters. Yamoaka et al. (2002) reported an aerial photo of the tidal vortex pair generated in the Neko-Seto Channel. Inman et al. (1971) reported an excellent aerial photograph of evenly spaced rip currents in a surf zone.

Another factor that causes surface roughness contrast is the accumulation along a line of surface debris, seaweeds, surface pollutants, oil slicks, and the like, which are drawn into the convergence zone as a result of horizontal convergence of surface water. If there is a surface convergence in the circulation pattern, the near-surface water is pulled into the line of convergence and is then drawn down into deeper depths. However, the up-thrust on the floats prevents them from sinking down with the current. This

causes the floating materials at the surface to be concentrated at the sea surface along the line of convergence. Conversely, a divergence zone results in a weakening or removal altogether of any floating material on the surface. A combination of convergence and divergence cells, such as those associated with Langmuir circulation, causes floating materials to be distributed on the sea surface in coherent rib patterns. Trapping of Sargassum weeds along the lines of convergence of Langmuir circulation cells and frontal regions is a familiar phenomenon. Furthermore, turbulence generated at the convergence zones adds to the surface roughness, which can be photographed. Thus, aerial photography of sea surface permits imaging of patterns resulting from some of the dynamic processes in the upper ocean. It is evident that aerial photography plays an important role as a seawater flow pattern visualization technique. Aerial photographs have also been valuable in detection of the boundaries of discrete water masses.

5.2. REMOTE DETECTION BY RADIOMETERS

Radiometers have been used extensively in the remote sensing of seawater current circulation features such as gyres, meanders, fronts, rings, upwelling, jets, and intrusions. The underlying principle in the use of radiometers for such studies is the fact that these features exhibit certain sea surface signatures such as color, temperature, or roughness that can be detected by radiometers.

In the oceanographic context, the radiometer is a sensor capable of measuring the flux of electromagnetic energy that impinges on it from the sea surface. Radiometers are employed to measure fluxes in the visible, infrared, and microwave bands of the electromagnetic spectrum and can be broadly classified into passive and active sensors.

Passive radiometers operate based on the principle that all materials that have temperatures greater than absolute zero (i.e., -273°C) emit electromagnetic radiation, the intensity and spectral compositions of which are functions of the physical properties of the emitting surface. An active radiometer illuminates the sea surface with its own energy. The energy scattered back from the sea surface in the direction of the sensor is processed to generate images and thereby elucidate the surface manifestations of seawater motion signatures. Various types of radiometric technologies that are employed for studies of such signatures are briefly discussed here.

Frontal and ring-dominated regions are associated with upwelling. In the upwelling process, the cooler and nutrient-rich water brought to the photic zone leads to greatly enhanced productivity of phytoplankton (known as a *phytoplankton bloom*) relative to that in the adjacent water masses. Phytoplankton (unicellular plants living in the sunlit

sea surface layers) contains a variety of light-absorbing photosynthetic pigments. The most abundant pigment is chlorophyll-a, which absorbs most strongly in the blue part of the optical spectrum (near 443 nm), with a secondary absorption peak at red wavelength (near 670 nm), whereas accessory pigments have absorption maxima at intermediate wavelengths. This absorption causes the solar radiation backscattered out of the sea at 443 nm to decrease rapidly with increasing chlorophyll-a concentration. The chlorophyll-a absorption is much weaker at 520 to 550 nm (the green part of the spectrum). Thus, waters that are poor in chlorophyll-a will appear as deep blue in sunlight, whereas waters rich in chlorophyll-a will appear green (Gordon et al., 1980).

The influence of phytoplankton pigments on the color of the seawater under natural light has been discussed by Yentsch (1960). Thus, seawater color contrast over a spatial domain on the sea surface is one of the water-motion signatures (upwelling) detected by a visible-wavelength radiometer. Sea surface color is expressed as the spectral (i.e., wavelength) composition of radiance exiting the sea surface in the visible waveband (approximately 400–700 nanometer). The sea surface color is dependent on the absorption and scattering properties of the water as well as dissolved and particulate constituents such as organic matter, phytoplankton cells, and suspended mineral particles.

Phytoplankton can also be excited by laser radiation to induce fluorescence in the red region of the spectrum. Thus, phytoplankton bloom, often representative of dynamic subsurface seawater motion extending up to the surface layers, has a color signature under natural as well as induced radiations. Time-series images of the ocean color contrasts permit an experienced oceanographer to study the evolution, growth, movement, and ultimate decay of these dynamic features. This is the basis underlying the use of visible wavelength radiometers for remote sensing of seawater motion signatures.

Passive as well as active sensing technologies have been used in visible-wavelength radiometers. The satellite-borne Coastal Zone Color Scanner (CZCS) and aircraft-borne oceanographic LiDAR (AOL) are, respectively, examples of passive and active radiometers.

5.2.1. Passive Radiometry in the Visible-Wavelength Band

The visible-wavelength passive radiometer measures the color of the sea surface under natural light. As mentioned earlier, this color is recognized as one of the manifestations of sea surface motion. The term *color* is used here to mean the spectrum of upwelling radiance just beneath the sea surface.

The possibility of remote sensing of the ocean color was demonstrated first by aircraft-borne radiometers (Clarke

et al., 1970). Subsequently, in October 1978 the CZCS was flown on the Nimbus-7 satellite on a “proof-of-concept” mission. The CZCS was the only sensor in orbit specifically designed to detect the upwelling solar radiance reflected from within the ocean.

The CZCS was a spatially imaging multispectral scanner (MSS). The MSS systems operate on the principle of selective sensing in multiple spectral bands. Accordingly, they are designed to sense radiation energy in a number of narrow spectral bands simultaneously. By analyzing a scene (feature) in several spectral bands, it becomes feasible to distinguish the color identity of the scene.

A commonly used scanning device is a rotating or oscillating mirror which moves the field of view along a scan line perpendicular to the direction of flight. At any instant in time, the scanner has an instantaneous field of view (IFOV). The IFOV is usually expressed as the cone angle (β) within which the incident radiation is focused onto the detector and is given by $\beta = \frac{D}{H}$ radians, where D is the diameter of the ground footprint and H is the flying height (see Figure 5.1). The rotating or oscillating mirror causes the IFOV to move from one side of the satellite flight path to the other. This allows the radiometer to scan a strip of the sea surface perpendicular to the flight path. The width of this strip below the radar is equal to the diameter, D , of the instantaneous footprint (see Figure 5.2). A consequence of increased swath angle is continuous increase of the footprint size as the IFOV moves outward from the satellite’s nadir. This happens because as the swath angle increases, the range between the satellite and the radiometer footprint increases. Consequently, the width of the strip (on the sea surface), perpendicular to the flight path, gradually increases as the distance from the satellite’s nadir increases. The forward motion of the satellite advances the viewed strip between successive scans,

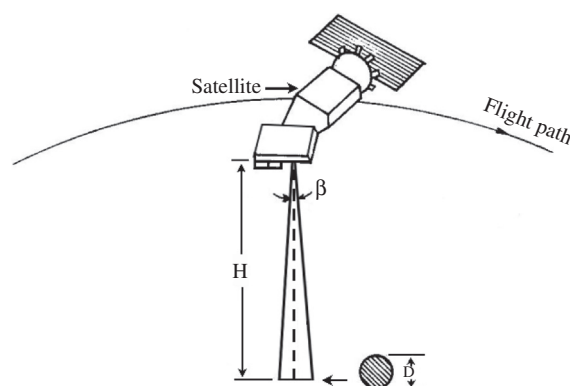


FIGURE 5.1 Schematic diagram illustrating the instantaneous field of view of a satellite-borne radiometer in relation to flying height, H , and beam width, β .

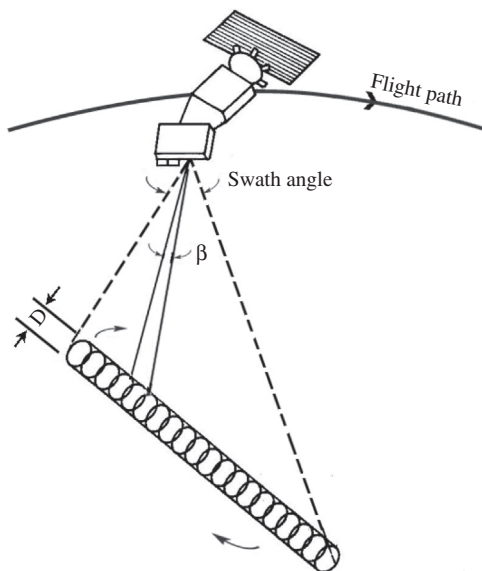


FIGURE 5.2 Schematic diagram illustrating a strip on the sea surface viewed in a single scan of a satellite-borne scanning radiometer.

causing a two-dimensional image dataset to be recorded (see Figure 5.3). For simplicity, the strip is shown to be of the same width.

The CZCS multispectral scanner had a geometric IFOV of approximately 0.05° . This corresponds to an area of a circle of approximately 830 m diameter on the sea surface from an altitude of 955 km. The scan was $\pm 39.32^\circ$ about the nadir, corresponding to a swath width of 1,659 km. Two

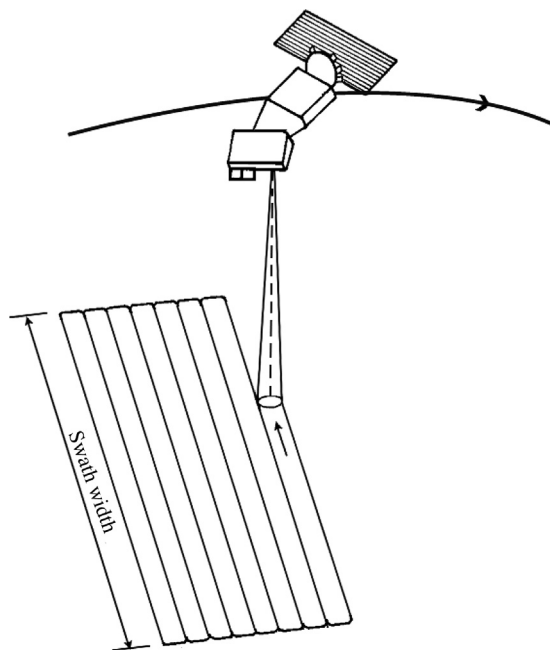


FIGURE 5.3 Schematic diagram illustrating the method of obtaining a two-dimensional image dataset from the sea surface using a satellite-borne scanning radiometer.

minutes of alongtrack scanning was packaged as an image for the purpose of data storage. With an orbit period of 104.15 minutes, this corresponded to a distance along the subsatellite track of 767 km. Thus, each two-minute image corresponded to an area of $767 \times 1,659$ (roughly a million) square kilometers. The image was slightly oversampled, and there were 1,968 pixels per scan line and 970 scan lines per image. The power available for sensor operation was limited; hence the CZCS was in use for only two hours per day (Austin, 1979). The CZCS incorporated a novel mechanism whereby its scan plane could be tilted up to 20° from nadir ahead of or behind the direction of travel of the satellite in 2° increments. This mechanism avoided masking a large area of the satellite field of view by sunglint (i.e., specular reflection of sunlight from the sea surface). The gain of the sensor and its tilt angle were controlled from the ground and, in normal operation, were determined by the solar elevation at the center of the scene (Gagliardini et al., 1984).

In an MSS system, the total incoming radiation is separated into several spectral components and is then sensed independently. A dichroic grating is used to separate the nonthermal wavelength from the thermal wavelength in the incoming radiation. The nonthermal wavelength component is directed from the grating through a prism or diffraction grating that splits the energy into a continuum of UV, visible, and IR wavelengths. At the same time, the dichroic grating disperses the thermal components of the incoming signal into its constituent wavelengths. By placing an array of detectors at the proper geometric positions behind the “dispersing” devices, each spectral band can be measured independently.

Silicon photodiodes and charge-coupled devices (CCDs) are the commonly used detectors in the visible region of the spectrum. Photodiodes are very sensitive light detectors whose output voltage varies linearly with the incident light intensity. Integrated photo-detector arrays with many photodiode elements are usually employed. A CCD is a microelectronic silicon chip that detects light. When light strikes the CCD’s silicon surface, electric charges are produced. The magnitude of the charge thus produced is proportional to the light intensity and exposure time. CCD arrays containing thousands of CCD elements are being employed in a number of different types of remote sensing systems because of their small size and weight, durability, and light sensitivity. The CCD receivers are designed for photo-electric scanning. Scanning is performed via a simple shift operation, reading sequentially through the array, because the sensor elements are coupled electrically as a shift register. CCDs have the advantage of wide dynamic range combined with rugged construction.

The CZCS scanning radiometer viewed the ocean in several spectral bands. These included bands in the visible,

near-infrared, and thermal regions of the spectrum. The visible bands were optimized for ocean color observations with narrow bandwidths placed in high, medium, and low regions of the chlorophyll absorption spectrum. The four visible bands were 443 ± 10 nm (blue), 520 ± 10 nm (green), 550 ± 10 nm (yellow), and 670 ± 10 nm (red). These very narrow bands (20 nm wide) were meant for discrimination of very subtle water reflectance differences. High signal-to-noise (S/N) ratio and high sensitivity enabled differentiation of slight changes in water-leaving radiances. The near-infrared channel (750 ± 50 nm) was meant to aid in locating cloud and water-land boundary prior to processing the data in the other bands (Lillesand et al., 1987). Because near-infrared radiation is not influenced by plant pigments but is strongly reflected from suspended sediments (Stumpf and Tyler, 1988), visible-band passive radiometry is also used for investigation of transport of suspended sediments in estuaries. Sediment patterns reveal residual transport, tidal streams, and small gyres (Robinson, 1985). The thermal infrared channel ($10.5\text{--}12.5$ μm) permitted measurements of sea surface temperature.

There are many factors that influence the quality of the data generated by an MSS system. Because these systems are designed to sense energy over a very small IFOV (to optimize spatial resolution) and in narrow wavelength bands (to optimize spectral resolution), a very limited amount of energy is incident on each of the individual detectors of the MSS system. This means that the detectors must be very sensitive to output a signal, which is significantly stronger than the level of system noise. The S/N ratio of an airborne MSS system is expressed as follows (Lillesand et al., 1987): $(S/N)_\lambda \propto D_\lambda \beta^2 (H/V)^{1/2} \Delta\lambda L_\lambda$. In this expression, D_λ is detectivity, β is instantaneous field of view, H is flying height, V is satellite velocity, $\Delta\lambda$ is spectral bandwidth of the channel, and L_λ is spectral radiance of ground feature.

Of these parameters, D_λ is a measure of the performance quality of the detector. The parameters β , H , and V together determine the spatial resolution, and $\Delta\lambda$ is a measure of spectral resolution. It is seen that the S/N value is partially based on wavelength-dependent parameters. Accordingly, different S/N values are applicable to each channel of an MSS system. Other factors that influence the S/N performance of any given scanner system are atmospheric attenuation, design of the system's optical components, and the noise characteristics of the system electronics.

In the CZCS scanner, the continuous electrical output from the detectors were digitized at such a rate that successive samples, or picture elements, represented contiguous areas on the sea surface. The angular size of the aperture was such that the forward motion of the spacecraft allowed successive adjacent scan lines of data to be added (Holligan et al., 1989). The CZCS radiance data was 8-bit

digitized onboard. The Nimbus-7 contained three onboard tape recorders. With these, it was possible to acquire imagery for areas out of range of the land-based receiving stations.

Data received from the Nimbus-7 CZCS visible bands were processed to a certain level at NASA (Hovis et al., 1980). The first level of processing converted the digital counts to radiances. Through NOAA, the timestamped and geocoded digital data are available to users on computer-compatible tapes (CCTs).

The depth to which the CZCS could "see" into the ocean was typically 15–30 meters in the open ocean. For relatively high pigment or turbid waters, it was generally less than 15 m at the most penetrating wavelengths. In certain coastal regions, large concentrations of sediments and dissolved organic substances from land runoff rendered the penetration depth even less than a meter. Thus, the remotely sensed signal represented a depth-weighted average of surface properties (Smith et al., 1987; Holligan et al., 1989).

During its travel to the visible-band passive radiometry sensor, the water-leaving radiance was considerably absorbed and scattered by the ozone layer. Furthermore, the atmosphere scattered light into the field of view of the sensor. Thus, only a small portion of the radiance received at the sensor aperture represented the radiance actually originating from the sea surface. In fact, the phytoplankton spectral signature represented less than 20% of the overall upwelling signal that reached the satellite sensor. This made it necessary to correct the data for atmospheric influences. Extraction of water-leaving radiance from the contaminated total radiance is a problem of remote sensing. Details on this topic may be found in Gordon et al. (1980), Sturm (1981), Gordon et al. (1982), Smith and Baker (1982), Robinson (1985), and Holligan et al. (1989).

After suitable atmospheric corrections of reflectances from various visible-band channels of the sensor, appropriate algorithms are applied to derive phytoplankton pigment concentration. Subsequently, color composite images are produced on a color video monitor of the image-processing computer system. Different colors are then attributed to different pigment concentration ranges. This permits the viewer to obtain a clear overall view of phytoplankton distribution. In many cases, the differences in ocean color may be used as a biological tracer or indicator of water mass origin when physical parameters give diffuse or conflicting signals (Tyler and Stumpf, 1989).

The initial imagery from Nimbus-7 satellite confirmed that the radiometer data could be processed to a level that reveals subtle variations in the concentration of phytoplankton pigments. The potential of visible-band passive radiometry imagery for the study of water mass boundaries and mesoscale seawater circulation patterns had been predicted by Hovis et al. (1980).

Today, sea surface color imaging is considered one of the potential techniques for remotely sensing oceanic water motion patterns. Through analysis of cloud-free radiometric images, Caraux and Austin et al. (1983) demonstrated that satellite remote sensing of chlorophyll could disclose characteristic seasonal phytoplankton patterns associated with hydrodynamic features such as coastal upwelling, river plumes, and offshore cyclonic activity. The passive radiometry image contains the most salient features of an eddy. For example, the chlorophyll concentration in the center portion of a warm-core ring (eddy) is depressed relative to the high-velocity boundary (Smith et al., 1987). The congruence between the physical and biological structure of the ring was remarkable. The ocean color imagery is indeed an interesting source of information for investigating upwelling motions.

Smith et al. (1987) have provided excellent CZCS images of two warm-core rings developed in the Gulf Stream/Sargasso Sea off the east coast of the United States. Analysis of successive images permits investigation of seasonal changes of oceanic boundaries. Once an image of a dynamic feature is obtained on a geographical map, it is possible to make quantitative measurements of the spatial features, which are apparent in imagery. The dominant length scales of isolated gyres are sometimes assessed by measuring with a ruler on a hard copy of the image. Looking at the whole scene, the human brain tends to automatically filter out or ignore irrelevant patterns. The speed and direction of movement of the identified feature, as well as its spatial growth or decay over time, may be studied from a sequence of images in the vicinity of the given area. Analysis of radiometer-derived images could reveal Gulf Stream meander and the rings shed by it.

5.2.2. Active Radiometry in the Visible-Wavelength Band

Interpretation of ocean color differences, especially for quantitative information, is often difficult because of interfering effects from the atmosphere. The atmosphere also produces spectrally dependent attenuation of the sea-scatter return and an overlapping upwelling radiance of its own. The effects of interfering signals can be reduced by using the pulsed nature and narrow spectral bandwidth radiation of a laser transmitter. A light detection and ranging (LiDAR) transmitter is an ideal pulsed illuminator for fluorescence studies because much of the optical background can be eliminated by time gating the receiver at the proper platform-to-surface range. Oceanographic LiDAR systems are used to make rapid, wide-area measurements from airborne platforms.

With excitation at an appropriate wavelength, natural waters are found to exhibit fluorescence from a number of naturally occurring substances, including chlorophyll,

algae, dye tracers, and pollutants, and the fluorescence emission spectra can be distinctive (Philpot and Vodacek, 1989). *Fluorescence* in this context refers to the characteristic of various objects on the sea surface to absorb energy at one wavelength and then emit a lower energy at different wavelengths shortly after excitation by the original energy source. Because different materials tend to fluoresce at different wavelengths, laser-induced fluorescence (LIF) can be used to discriminate among material types. Laser fluorescence makes use of this property. Because fluorescence intensity is usually proportional to the concentration of the fluorescing material, the LIF technique is potentially used to detect and measure the concentration of various fluorescing substances. Material particles in the ocean waters are passive tracers of water motions. Time-series spatial images of these substances permit identification and quantification of seawater motion. This is the basis underlying the use of a visible-wavelength active radiometer for detection of ocean dynamic features. LIF is routinely used for airborne monitoring of chlorophyll and is a potential technique for remote sensing of coastal ocean dynamics.

The active sensor used in the LIF remote sensing technique is a LiDAR system. In this technique, a pulsed laser is used to illuminate the top layers of the sea surface, and a multichannel fluorometer (spectroradiometer) records the spectral characteristics of the radiation emitted by the fluorescent objects in the water. The fluoresced radiation is often focused by a lens onto the entrance slit of a spectrograph (an optical grating). The spectrally dispersed light from the spectrograph is detected with a multichannel photodiode array and the associated active elements. The spectrum is usually corrected for instrument sensitivity and configuration.

Aircraft-borne oceanographic LiDAR (AOL) systems have been used operationally to map chlorophyll concentration and, therefore, circulation features of coastal seawater bodies. A conceptual rendering of an AOL system is given in Figure 5.4. Smith et al. (1987) used an AOL for detection of a Gulf Stream warm-core ring. In this system a pulsed laser with a wavelength of 532.1 nm (green) was used to stimulate fluorescence from the chlorophyll and phycoerythrin photopigments in phytoplankton from a subsurface water column within a footprint of ~ 0.5 m diameter. The LIF from these photopigments, centered at 685 nm (red) and 580 nm (yellow), respectively, were received and recorded. Along with the laser-induced fluorescence, the LiDAR recorded the short-range distance between the aircraft and the sea surface. The aircraft position was determined from an inertial navigation system.

The distinct and important characteristic of an active spectrometer is its specificity. The laser's spectral bandwidth is sufficiently narrow (typically subnanometer) to

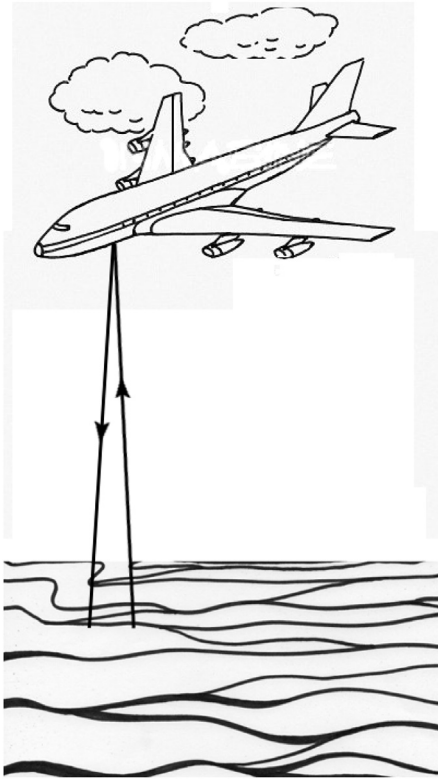


FIGURE 5.4 Conceptual rendering of an aircraft-borne LiDAR system.

allow identification of spectral lines, which are easily resolved and unambiguously assigned to chlorophyll and phycoerythrin pigments in the phytoplankton.

5.2.3. Passive Radiometry in the Thermal Infrared Band

The use of thermal infrared radiometry for detection of seawater circulation features relies on the fact that some of these features often have a thermal signature. For example, western boundary currents (WBCs) are associated with recognizable surface temperature gradients. Well-known WBCs, such as the Gulf Stream and the Somali Current, are known to have distinct surface temperature gradients. As the name suggests, well-known circulation features such as warm-core and cold-core eddies, warm-water and cold-water jets and intrusions, fronts, and the like provide distinct spatial sea surface temperature (SST) gradients. For coastal waters, the spatial temperature gradients are often indicative of advective motions of estuarine waters. The estuarine water advection gives rise to relatively sharp horizontal gradients at the frontal boundary of warm stratified water and cool tidally mixed waters. Similarly, the upwelled waters are cooler than the surrounding surface waters. The boundary between the cooler upwelled water and the surrounding warmer surface water often takes the form of a sharp front, which can be

readily detected from sharp variations in spatial SST. In the case of water currents and intrusions, frequent monitoring of the leading edge of the SST boundary allows one to estimate the variability of their speed and direction. In the case of meanders and detached eddies, such monitoring permits determination of their spatial scales and shape as well as speed and direction of their drifts.

The sea surface temperature is remotely measured from ships, aircraft, or satellites by observing the intensity of the infrared radiation (within the wavelength range 8–14 μm) emitted from the sea surface. The radiated energy is an external manifestation of the thermal energy state of the water molecules that constitute the sea surface. The radiated energy is a function of its “radiant” temperature. Because the absorption in seawater at the infrared wavelength is rather high, only the radiation from a very thin surface layer (less than one-tenth of a millimeter) is radiated into the atmosphere.

Remote measurement of SST relies on the Stefan-Boltzmann law, which states that the total radiant exitance, M , from the surface of a black body varies as the fourth power of its absolute temperature. The *black body* is a hypothetical radiator that totally absorbs (i.e., no reflection) and reemits the entire energy incident upon it. The Stefan-Boltzmann law (applicable for a black body) is expressed in mathematical form as $M = \sigma T^4$, where M is the total radiant exitance in W/m^2 ; σ is the Stefan-Boltzmann constant; and T is the temperature of the black body ($^{\circ}\text{K}$).

The concept of a black body is only a convenient theoretical vehicle to describe radiation principles. Real bodies do not behave as black bodies; they emit only a fraction of the energy emitted from a black body at the equivalent temperature. However, blackbody radiation principles can be extended to real bodies by reducing the radiant exitance, M , by a factor termed *emissivity*, ϵ , such that for real bodies $M = \epsilon \sigma T^4$. The emissivity of a material is its emitting ability relative to that of a black body.

By definition, ϵ is the ratio of the radiant exitance from an object at a given temperature to that from a black body at the same temperature. The emissivity can have values between 0 and 1. It can vary with wavelength and viewing angle. Depending on the material, emissivity can also vary somewhat with temperature. At thermal infrared wavelengths, the emissivity of water varies from 0.96 to 1.00; therefore, its behavior is very close to that of a blackbody radiator. The temperature T of a radiating surface can be inferred by remote measurements of the radiant exitance, M , from the surface. This indirect approach is used for remote sensing of sea surface temperature. M is measured over a discrete wavelength range. The 8–14 μm region of the spectral radiant exitance curves is of particular interest because it contains the peak energy emissions for most ocean surface features.

5.2.3.1. Detectors

Infrared radiance detectors can be classified into two types: heat-sensing and photon-sensing devices. Heating of a material or the absorption of photons by a semiconductor can both produce changes that can be detected by appropriate electrical methods. Thermal detectors respond to the total energy of the radiation impinging on them, irrespective of its spectral distribution, whereas photon detectors respond to the rate at which quanta of radiation are absorbed (Katsaros, 1980). Thermal detectors such as thermistor flakes were used in shipborne radiometers. A major disadvantage of thermal detectors is their comparatively long response time. For this reason they are rarely used from fast-moving vehicles such as aircraft and satellites. Contrary to thermal detectors, photon detectors are capable of very rapid ($<1 \mu\text{s}$) response. With their rapid-response characteristics, photon detectors are in widespread use in satellite-borne remote sensing systems. The photoconductive effect is commonly used in photon detectors. Increase in conductivity results when the energy of a photon induces free flow of electrons, or “holes,” or electron-hole pairs within the crystal lattice. Detection of infrared radiation is enhanced if the background thermal excitation is minimized. For this reason semiconductor photon detectors are usually operated at temperatures approaching absolute zero. Normally, the detector is surrounded by a Dewar containing liquid helium or nitrogen (-196°C). Electrical (Peltier) cooling can also be used. The commonly used photon detectors are mercury-doped germanium, Indium antimonide, and mercury cadmium telluride (Lillesand et al., 1987).

In remote sensing, images of sea surface temperature contrasts are interpreted in terms of sea surface current patterns (Harris et al., 1978, Legeckis, 1987). Two-dimensional thermal images can be produced either by an array of detectors or by a scanning radiometer. Airborne radiometers are usually configured as scanners. In this configuration, only one detector is used. The target area is scanned either by a rotating mirror or by the spin-and-advance-motion of the satellite. In the spin-stabilized TIROS-series satellites, the detector views the Earth from horizon to horizon in lines perpendicular to the path of advance. In the Nimbus series, the same side of the satellite always faces the Earth, and the scan is provided by a rotating mirror. The radiation emitted from the scene is intercepted by the scan mirror, which diverts the radiation to a collecting telescope. The telescope focuses the radiation to a detector. In a normal case, the scan mirror is inclined 45° to the optical axis. When the scan mirror is rotated about the optical axis, the field of view of the telescope sweeps out a circle in a plane, which is normal to the rotation axis of the scan mirror. Thus, by the scan mirror rotation, radiation is received and measured from

a continuous line of length corresponding to the total scan angle. When such an instrument is mounted on a moving platform (spacecraft) with the optical axis parallel to the platform motion, the motion of the platform produces successive scan lines, giving contiguous imagery. In the case of a multispectral scanner, the energy collected by the telescope is channeled to a spectral dispersing system (spectrometer) to be registered in different spectral bands.

In operation, the thermal energy radiated from a footprint on the sea surface is focused onto the detector, which converts the thermal radiation into an equivalent electrical signal. Because glass lenses absorb thermal infrared radiation, either a germanium lens or a set of gold-coated mirrors of suitable shapes is used to focus the radiant energy onto the detector. Gold is a good reflector of infrared radiation. The entering radiation comes alternately from the sea surface footprint and from an onboard temperature reference source (blackbody cavity) via a rotating toothed chopper wheel in front of the focusing system (see Figure 5.5). The radiation from the target reaches the detector through the openings between the chopper teeth. The chopper's gold coating acts as a mirror when the chopper covers the focusing system. This allows reflection of the radiation from the blackbody cavity onto the detector. Chopping of the radiation produces an alternating signal. The blackbody cavity is an electrically heated, calibrated internal temperature reference source. The electrical signal from the detector is processed so that its amplitude is related to the difference in the intensities of

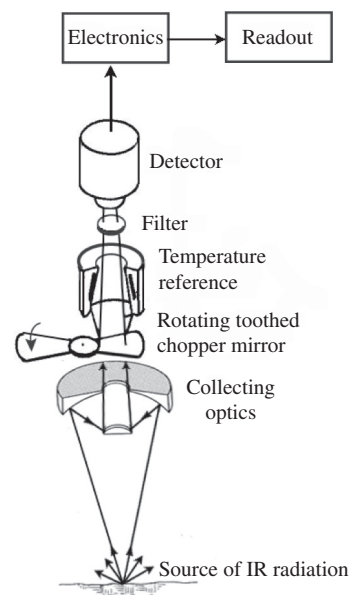


FIGURE 5.5 Schematic diagram illustrating satellite remote sensing of thermal infrared radiation from the terrestrial surface with reference to an onboard temperature reference source. (Source: In part from Lillesand and Kiefer, 1979.)

thermal radiation from the terrestrial (sea surface in the present case) footprint and the blackbody reference source.

5.2.3.2. Atmospheric Effects and Correction

Several environmental factors tend to degrade the accuracy of the perceived SST. The atmosphere has a significant effect on the intensity and spectral composition of the energy recorded by a thermal system. The intervening atmosphere between a thermal sensor and the sea surface can increase or decrease the apparent level of radiation coming from the sea surface. The atmospheric absorption and scattering of the signals from the sea surface tend to make the sea surface appear cooler than it is, and atmospheric emission tends to make the sea surface appear warmer than it is. Depending on atmospheric conditions during imaging, one of these effects will outweigh the other, thereby resulting in a biased sensor output (Lillesand et al., 1987). Thus one of the initial problems in making SST observations from space used to be the obscurity of the sea surface by clouds. The presence of noise levels of various satellite instruments has been another problem. However, techniques have been developed to correct for these effects (La Violette et al., 1969; Shenk et al., 1972; Hillger et al., 1988).

Several methods exist for atmospheric correction. A multispectral technique is one among them. The effects of varying water vapor concentration on the integrated atmospheric transmittance differ over different infrared spectral channels. Consequently, the differences of the perceived SST between different channels may be used to implement correction for errors induced by water vapor. Another method is to use different algorithms for processing of data from night and day. This method relies on the fact that atmospheric contributions are different at night from daytime ones. There is no reflected solar radiation at night. The daytime corrections should strictly include a dependence on the sun's zenith angle. Another major improvement in accuracy is promised from the use of a multilook sensor, which views the same piece of sea surface through different atmospheric path lengths (Robinson, 1985). The presence of clouds was a serious problem in frontal detection. However, the fact that the clouds are almost always colder than water and that they move much more rapidly than sea surface water motion features have become useful in resolving this problem. The effects of clouds are now being reduced by overlaying several daily pictures and compositing them by selecting the warmest temperatures at each point. Using this method, cloud effects have been eliminated entirely or reduced substantially in many pictures. When the clouds are extremely persistent, the process of overlaying can be extended to several days. This latter process may degrade the results because corresponding points can represent temperatures from different

days, but it has produced usable images from very poor data (Gerson et al., 1982).

5.2.3.3. SST Imaging

Beginning in 1978, passive radiometers onboard NOAA environmental satellites provided synoptic views of the sea surface temperature several times a day, with a spatial resolution of 1 to 4 km. For example, Vigan et al. (2000) reported SST images over the Gulf of Mexico and the Agulhas Current waters off South Africa. Examining SST image sequences makes it possible to track the evolution of fine-scale oceanic patterns possibly associated with strong currents. Satellite-based surveying methods benefit from high space/time resolution of radiometer data (1–4 km by 1–4 km every four to six hours) and from their synoptic spatial coverage (1,000 by 1,000 km), which sets up the possibility for short-term forecasting (48–72 hours) of ocean features evolution. This, together with cost effectiveness, contributes to making satellite-based methods superior to onsite approaches.

Vigan et al. (2000a, b) presented a variable finite-element model for the purpose of computing absolute upper-layer oceanic currents from sequences of advanced very high-resolution radiometer (AVHRR) sea surface temperature images. Satellite images have been processed daily and current-calculation algorithms and feature-tracking tools have been applied, yielding a detailed report of oceanic conditions. Comparison with simultaneously collected current measurements from an ADCP demonstrated the outstanding accuracy of the satellite-based approach. The oceanic current calculations were found to be accurate to within 10% in magnitude and 10° to 15° in direction after a comparison to simultaneous onsite current measurements.

The model is not only diagnostic but has predictive skill as well, making it a powerful tool regardless of atmospheric conditions. These researchers have also developed feature detection and tracking tools (fronts, eddies, filaments, plumes, etc.) based on satellite imagery. Tracking an oceanic front from an image series allows, for example, the monitoring of typical quantities such as frontal-wave propagation velocity or its surging or shedding, which provide forecasting clues for a 48- to 72-hour prediction of the upper-layer currents.

It was found that the calculation of currents from time-series satellite-derived SST imaging is applicable to any oceanic province featuring relatively pronounced temperature variations over space and time, typically in the Gulf of Mexico, off the U.S. east and west coasts, north and southeast Brazil, Argentina, South Africa, Namibia, or Angola, but also in the China Sea, in Indonesia, or east of Australia. As typical examples, Figures 5.6 and 5.7 show, respectively, a satellite AVHRR infrared image of a Gulf Stream frontal eddy in April 1977 and a NOAA/satellite AVHRR thermal

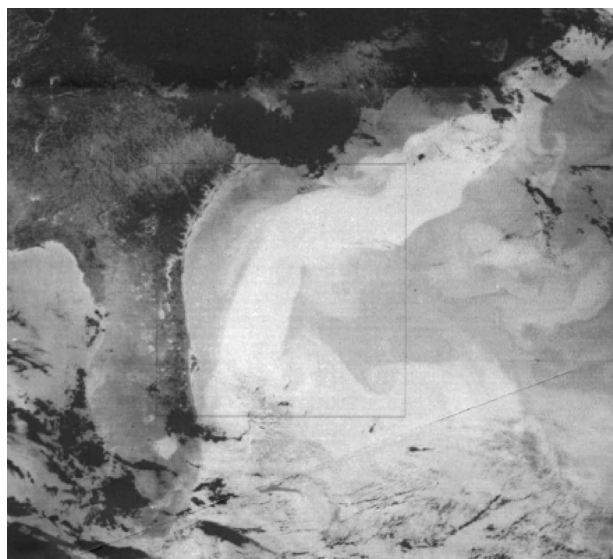


FIGURE 5.6 Satellite AVHRR infrared image of a Gulf Stream frontal eddy on 16 April 1977 at 0200 GMT. (Source: Lee *et al.*, 1981.)

infrared image depicting the structure of Norwegian coastal current in September 1995. Vigan (2002) provided AVHRR images of Loop Current warm waters and cold coastal water masses in the Gulf of Mexico during March 1996. Vigan (2002) also provided a July 2000 AVHRR image of the Agulhas Current waters that separate from the South African coast and flow toward the southwest describing meanders. Upper-layer current was calculated from two successive AVHRR images. Based on this calculation, the current magnitude in the Agulhas jet core was found to be about 4 knots. A METEOSAT infrared image of the meandering Agulhas Current reported by Irvine and Tilley (1988) also exhibited comparable features.

5.2.4. Microwave Radiometers

Remote sensing of the ocean surface by satellite-borne radiometers operating at visible and infrared wavelengths has provided valuable details of sea surface circulation features. However, the sea surface cannot be adequately viewed by visible-wavelength radiometers in darkness. Likewise, SST-derived information is obscured by cloud cover. Operational utility of these sensors is thus limited because much of the sea surface either is obscured by clouds or is in darkness. In contrast, frequencies in the microwave band have the unique capability of propagating through clouds. Also, they do not depend on the sun's illumination and therefore can operate during day and night (Calla, 1984). The ability of radiation in the microwave band to propagate through clouds renders microwave sensors effective all-weather devices, although water in the form of precipitation scatters radiation and can render the atmosphere opaque at the microwave band (Robinson, 1985).

The microwave radiometer is the passive counterpart to microwave radar. Being passive, the microwave radiometer does not supply its own radiation; rather, it senses the naturally available microwave energy within its field of view. Microwave sensing principles and sensing instrumentation are similar to those of thermal infrared sensing in many respects. As with thermal infrared sensing, black-body radiation theory is the principle used in the operation of microwave radiometers, and both kinds of radiometer sense the sea surface temperature for detection of sea surface manifestations of seawater circulation features. The main difference between thermal infrared radiometers and microwave radiometers is that the former uses photon detection elements whereas the latter uses microwave antennae for detection of radiation emanating from their field of view.

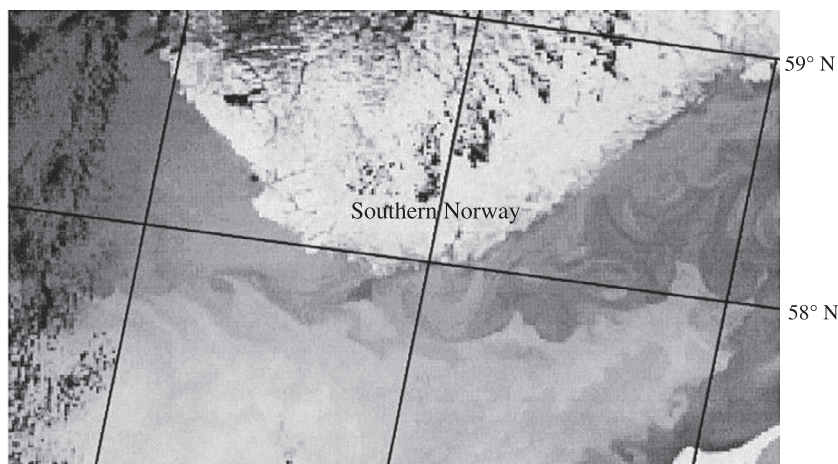


FIGURE 5.7 NOAA/Satellite AVHRR thermal infrared image depicting the structure of Norwegian coastal current on 20 September 1995. (Source: Johannessen *et al.*, 2000.)

5.2.4.1. Principle of Passive Microwave Radiometry

Passive microwave radiometry applied to investigation of SST involves the detection of thermally generated radiation from the sea surface at microwave frequencies. The spectral band in which passive microwave radiometry applies is approximately 1 GHz to 200 GHz, i.e., a wavelength of approximately 30 cm to 0.15 cm. Remote sensing of SST from air- and space-borne passive microwave radiometers relies on Planck's radiation law. If the temperatures to be measured lie in the vicinity of 300°K (typical of Earth's surface temperatures), and the radiation of interest is in the microwave region of the electromagnetic spectrum, the spectral radiance or brightness of the radiating body is often expressed by the Rayleigh-Jeans approximation of Planck's blackbody radiation law. This approximation is given by $B_f(\theta, \phi) = \frac{2kT}{\lambda^2}$, where $B_f(\theta, \phi)$ is the spectral brightness of the radiating surface per unit frequency of radiation in the conventional direction (θ, ϕ) ; k is Boltzmann's constant; T is the temperature of the radiating surface in °K; and λ is the wavelength of the radiating electromagnetic wave.

It is seen that for a given wavelength, the brightness is directly proportional to the temperature of the radiating source. The approximation given above applies to an ideal black body. Because an ideal black body does not exist in nature, measurements are usually given in terms of the "brightness," T_B . In passive microwave radiometry terminology, the brightness temperature is also called *apparent antenna temperature*. The brightness temperature of the radiation is equal to the temperature T_B of the equivalent black body. This leads to the relationship of brightness temperature to physical temperature T in terms of emissivity $\epsilon(\theta, \phi)$ as $T_B = \epsilon(\theta, \phi)T$.

Normally, the radiometer output is expressed in terms of T_B ; i.e., the system is calibrated in terms of the temperature that a black body located at the antenna must reach to radiate the same energy as was actually collected from the ground (Lillesand et al., 1987), which is sea surface in the present case. The emissivity term renders the just-mentioned relation applicable to real bodies. In the case of sea surface, the emissivity is in general a function of sea surface texture (i.e., sea state), temperature, chemical composition, and the radiating frequency. Below 5 GHz the emissivity, ϵ , of the sea surface at wavelength λ is expressed in terms of the molecular temperature of the sea surface, T_S , and chemical composition, S (salinity), of the surface water. Details on these aspects may be found in Blume et al. (1977).

The emissivity of the sea surface at the lower end of microwave frequencies (between 1.5 and 5 GHz) is approximately 0.3 instead of near-unity in the infrared region of radiation. This difference places stringent

requirements on the absolute accuracy of measurements by the microwave radiometer system. Because passive microwave sensors operate in the low-energy tail of the blackbody radiation curve for temperatures in the region of approximately 300°K (typifying SST features), the signal received at the radiometer antenna is extremely weak. This means that a comparatively large antenna beam width is required to collect enough energy to yield a detectable signal. Consequently, passive microwave radiometers are characterized by low spatial resolution.

5.2.4.2. Passive Microwave Radiometer Instrumentation

The first microwave radiometer was reported by R. H. Dicke in 1946. Most microwave radiometers in use today are similar in concept to the one designed by Dicke. The Dicke radiometer in its simplest form consists essentially of a high-gain microwave antenna with low side lobes, a microwave switching circuit (a Dicke switch), and the required detection and recording electronics. The microwave radiation of targets is very weak. The noise temperature of a receiver can reach several thousand times the radiation from the target. For this reason microwave radiometers must be designed to detect a weak signal in a large noise.

The equation for sensitivity of a Dicke-type radiometer is given by $\Delta T_{rms} = \frac{2T_{eff}}{\sqrt{\Delta f \tau}}$, where T_{rms} is the root-mean-square output of a radiometer defined as the sensitivity; Δf is the RF bandwidth; τ is the integration time; and T_{eff} is the effective noise temperature, including the temperature received by the antenna from the target and the temperature of the receiver converted to the antenna.

It can be seen from this relation that a low effective noise temperature and a wide RF bandwidth improve the sensitivity. In conventional microwave radiometers, the antenna picks up the very low-level microwave signal. The switching circuitry permits rapid, alternate sampling between the thermal radiation power received by the antenna and an internal calibration temperature reference signal. The reference load can be either a heated or cooled source or space. Space has a brightness temperature of approximately 3°K (Thomas, 1981). The differential signal is amplified and phase-detected synchronously with the switching circuit (Tomiyaasu, 1974). Through suitable calibration procedures, the difference between the antenna signal and the reference signal can be related to the input antenna temperature, which is a measure of the radiation intensity received by the antenna.

A passive microwave radiometer used for measurement of SST detects the radiation emitted from the sea surface and the intervening atmosphere. Quantitative measurement of thermal emission from the sea surface by a remote

sensing radiometer, operating from high altitude, requires that correction be applied for the radiative and transmission properties of the intervening atmosphere. At microwave frequencies there are four principal categories of interference that can be classified as atmospheric effects. They are (Blume et al., 1977):

1. Extra-terrestrial background radiation
2. Radiation from discrete stellar radio sources
3. Attenuation from oxygen and water vapor in a cloudless atmosphere
4. Attenuation resulting from rain clouds

For clear atmosphere, water vapor and molecular oxygen are the major sources of attenuation in the microwave band. Precision measurement of SST using a microwave radiometer requires that all unwanted side effects such as sky background radiation, atmospheric emission, antenna beam pattern, and instrument instabilities must be accounted for. Given the very weak signal that has to be measured by a microwave radiometer, thermal noise from the antenna and the other parts of the electrical signal pathway to the preamplifier is also a major problem to be circumvented. A conventional method of correcting the errors resulting from atmospheric effects is reception of thermal radiation at different wavelengths and polarization. The problem of high-frequency noise is overcome by integrating over many samples. Thermal noise is reduced by packaging the critical parts into a single integrated unit for isothermal operation.

Initial experiments using an airborne passive microwave radiometer demonstrated its feasibility for determining SST values. Blume et al. (1977) used an aircraft-borne, 2.65 GHz radiometer for the Chesapeake Bay area. The result was compared in detail with accurately obtained sea truth data. For a calm sea, the observed temperature agreed well with that calculated from the known sea surface and atmospheric properties. For cases in which the surface wind speeds were of the order of 7 to 15 knots, an excess temperature was observed. This was attributed to emissivity variations due to surface roughness and microscale surface disturbances. The passive microwave radiometer is now recognized as a useful tool for detection of ice floes. Time-lapse images of ice floes provide a means for quantitative estimation of seawater motions in ice-infested regions such as the Greenland Sea.

5.2.4.3. Scanning Multichannel Radiometers

A scanning microwave radiometer has the advantage of providing an SST map over a large area. Conceptually, a scanning microwave radiometer operates such that its antenna's field of view is transverse to the direction of flight. Transverse scanning can be performed either mechanically or electronically. Two major types of antenna used in passive microwave radiometry are dishes and phased arrays. A

typical mechanically scanning dish antenna is a parabolic dish with a suitable collecting horn. In the case of a multi-channel radiometer, the collecting horn may consist of a cluster of single-frequency horns or a single horn that receives the various frequencies coaxially (Thomas, 1981). In a phased array, multiple arrays of waveguide sections are employed. Using appropriate phase shifters, the antenna beam is electrically steered perpendicular to the direction of flight. Such an electrically scanning microwave radiometer (ESMR) was carried on the Nimbus-5 satellite, launched in 1972, and the Nimbus-6, launched in 1975. The former made use of a phased array antenna with linear polarization and operated at 19 GHz, whereas the latter measured both vertically and horizontally polarized components at a frequency of 37 GHz.

Retrieval of SST information from a passive microwave radiometer requires accurate known brightness temperatures at the antenna's collecting aperture at each frequency and polarization. The antenna receives radiation from all directions as weighted by the antenna patterns. The radiation received through the side lobes must be corrected in order to derive the true brightness temperatures emanating from the direction of the antenna boresight. Antenna pattern correction methods may be found in Njoku et al. (1980).

Passive microwave measurements from polar orbiting satellites provide global coverage of SST variability and thereby several sea surface circulation features. The first multichannel radiometer for remote sensing of terrestrial surface temperature was orbited onboard Soviet Cosmos-243 in 1968. Subsequently, a similar one was flown on Cosmos-384 in 1970. The Cosmos experiments included measurements at 8.5, 3.4, 1.31, and 0.8 cm wavelengths. The scanning multichannel microwave radiometer (SMMR) on board Nimbus-G and Seasat-A satellites measured thermal microwave emissions from the Earth at five dual linearly polarized frequencies (6.6, 10.69, 18, 21, and 37 GHz), from which SST values were derived. The SMMR instrument thus operated with 10 channels and vertical and horizontal polarizations at each of these five frequencies. Measurements were made over a swath 822 km wide below the Nimbus-G and 595 km wide below the Seasat spacecrafts. For a satellite orbiting at an altitude h , the ground resolution cell size d (i.e., the footprint on the sea surface) is given by the expression (Robinson, 1985) $d = (\lambda h)/D$, where λ is the wavelength of the received radiation and D is the antenna aperture diameter.

In practice, for a given altitude of the satellite orbit, a compromise is usually reached among footprint size, antenna size, and minimum frequency. Nimbus and Seasat SMMR had an antenna diameter of 70 cm and a highest frequency of 37 GHz (i.e., a lowest wavelength of 0.8 cm). The smallest spatial resolution cell was about 20 km at a wavelength of 0.8 cm and was proportionately larger at other wavelengths (Gloersen and Barath, 1977). For

example, the spatial resolution of the SMMR was about 100 km at 6.6 GHz. On Nimbus-G, the SMMR scan pattern was forward-viewing and scanned equally to either side of the orbital track so that the swath was centered on that track. On Seasat-A the SMMR scan pattern was aft-viewing and biased toward the right of the flight path so that the center of the swath was 22° from the orbital track. Data from the SMMR were gathered from footprints of different sizes for each of the frequency channels. The SMMR instrument consisted essentially of five hardware elements:

1. An antenna assembly consisting of a reflector and a multifrequency feedhorn
2. A power supply module
3. A scan mechanism
4. An RF module containing the input and reference switching networks consisting of Dicke-type switches and detection electronics
5. A post-detection electronics module

The mechanically scanning antenna system consisted of an offset parabolic reflector with a 70-cm diameter collecting aperture and a multifrequency feed assembly. The antenna reflector was scanned with a sinusoidally varying velocity over a 50° swath angle and with a 4-s time period (Njoku et al., 1980). The antenna beams produced contiguous footprints on the terrestrial surface. During most of the scan, the radiometric signal pertaining to SST consisted of data obtained from the sea surface. At one end of the antenna scan a “hot” reference source was observed; at the opposite end a “cold” source was observed. The hot source was a microwave guide termination at the instrument’s ambient temperature (approximately 300°K) and the cold source was provided by a special horn antenna viewing deep space (approximately 2.7°K). A modulator switch assembly alternated at approximately a 1-kHz rate between a reference temperature signal and an input signal.

The output of each channel—a voltage proportional to the difference between the radiometric signal and an internal reference source—was integrated over appropriate time periods, digitized, encoded, and sent to the spacecraft’s data system for transmission to ground. Measurements from a number of very accurate ($\pm 0.05^\circ\text{C}$) platinum resistance sensors, distributed at various critical points in the SMMR microwave circuitry, were combined with the telemetry datastream and transmitted to the ground. This combined dataset consisting of signal, hot calibration, cold calibration, and instrument temperature values was used to compute radiometric temperature values. The effective radiometric temperature is often referred to as *antenna temperature*. The antenna temperature was then corrected for antenna pattern effects to yield *brightness temperature*. These aspects have been discussed by Swanson et al. (1980). The SMMR retrieval algorithms have been discussed by Francis et al. (1983).

The SMMR was conceived to provide an instrument capable of obtaining (among other parameters such as surface wind speed) SST information, which is an important parameter required by oceanographers for developing and testing global ocean circulation models and other aspects of ocean dynamics. The goal of SMMR was accuracy better than 1.5°K in obtaining SST. The SMMR has indeed demonstrated sensitivities sufficient for determination of SST with an accuracy of 1°K or better, excluding conditions at significant rainfall. Because in studies of oceanic circulation features it is the difference in SST that is more important than absolute temperature, this accuracy is often sufficient for such studies. For example, owing to sharp temperature contrast between ice sheet and the surrounding water, the edge of the ice sheet is readily detectable on microwave imagery. In fact, SST studies using satellite-borne SMMR have been very useful in delineating sea ice in the Arctic and Antarctic waters (Robinson, 1985). The SMMR flown on the Nimbus satellite was able to record the movement and change in character of sea ice continuously over several years, despite cloud cover and the long polar night. Because icebergs are excellent Lagrangian tracers of water motion in the polar regions, SMMR is an excellent tool to monitor sea surface water circulation in these environmentally hostile regions. Even very slow motions can be detected using time-sequence SMMR imaging over long periods of time.

In the past, passive microwave technique has been used effectively to monitor circulation features in remote areas such as the Greenland Sea, day and night. SMMR images have been used successfully for investigation of the dynamics of the East Greenland Current, based on the creation of a mysterious large-scale ice cover phenomenon called *Odden*, in the Greenland Sea. Time-series of ice concentrations derived from the SMMR onboard the Nimbus-7 satellite have been used for this investigation. Odden is a large tongue of ice that typically appears once every year in the Greenland Sea at any time of the winter season as a result of a rather sudden decay of ice concentration solely along the shelf slope of Greenland, leaving the rest of the ice cover intact. The average size of this tongue may be 3–400 km from north to south and 1–200 km from east to west. The reason for the mysterious appearances of Odden remained largely unknown for many decades.

Close monitoring of the ice concentration in this region using data from the Nimbus-7 satellite in March 1979 indicated that Odden grew from 3–500 km in length at least within 48 hours. Based on meteorological and other data, it was argued that the process of the creation of Odden is neither a result of a current coming from the north nor a result of ice melting at the ice/air interface. These arguments led to the postulation of a vertical cellular circulation of warm water in the Greenland Sea, the driving force of which is the winds from north and northeast causing an

Ekman surface transport toward the east coast of Greenland. The proposed cellular circulation is believed to be the driving mechanism behind the formation of Odden in the Greenland Sea. It is interesting that a system inherently capable of observing solely the surface phenomena became instrumental in providing some interesting additional information about subsurface processes, which hopefully explains the mechanism behind the creation of the mysterious Odden. No wonder space agencies of various countries are including passive microwave radiometers in their ocean remote sensing programs.

5.3. ACTIVE MICROWAVE RADAR IMAGING OF SEA SURFACE CURRENT SIGNATURES

Apart from passive microwave radar imaging technologies discussed in the preceding sections, active microwave radar imaging technologies are also used in identifying sea surface water motion features. Active microwave imaging radar systems detect sea surface circulation signatures by utilizing (1) sea surface roughness contrast and (2) the sidelighted character of icebergs, which move under the influence of seawater current. The former is applicable anywhere in the ocean, but the latter is applicable only in high-latitude regions of the globe. In cases where no damping film material is present, the oceanic eddy features alter their expression into a bright radar modulation along the converging front. The indirect contribution from intermediate wave breaking via their influence on short-wind waves dominates the surface roughness modulation and thus Bragg-like scattering from the sea surface and the microwave radar image manifestation.

Radar image of the sea surface is simply a pictorial representation of the backscattering properties of the sea surface at the radar wavelength. Typically, the image is simply a photographic presentation of the backscattered signal intensity that is recorded as a function of antenna scan and slant range. The backscattered signal intensity is converted to a video signal and is usually recorded on photographic film as shades of gray ranging from black to white. These shades are known as *image tone*. The distribution of tone changes on an image is known as *image texture*. The texture is often classified as fine, smooth, coarse, grainy, speckled, mottled, irregular, and so forth. Image texture permits identification of features on an image. Because image texture depends on the distribution of tones, not on the absolute value of tones, texture is less affected by the lack of image calibration than is tone (MacDonald, 1980). For this reason, precise signal amplitude measurement is not usually necessary in radar imaging applications.

In photographic as well as radar imaging, interpretation of the picture is based on shape, texture, and context.

Production of images with good geometric fidelity and good contrast is more important than accurate calibration (Ulaby et al., 1982). Because the information content in an image is not dependent on absolute values of tones, the image texture of a given region at a given time remains relatively constant from one image to another, regardless of the radar system's gain settings.

The amount of power received by the radar from the sea surface (i.e., radar return) depends on the radar system properties and sea surface roughness properties. The former includes transmitted power, antenna gain, transmission wavelength, and slant range distance between radar and the "target" on the sea surface. The sea surface property is revealed by the scattering coefficient, also called the *normalized radar cross-section*, σ_0 . When radar system properties are held constant, the gray tone on the radar image is proportional to σ_0 , which, in turn, is determined by both the roughness and the electrical properties of seawater. The electrical properties of seawater do not vary appreciably from region to region. For this reason, dependence of radar return signal strength on electrical properties may be generally ignored in sea surface roughness measurement.

Surface roughness, as applied to microwave radar imaging, is a geometric property that determines the strength of the backscattered signal. The sea surface is often described statistically rather than deterministically. Scattering from statistically rough surfaces falls into two classes, namely a Bragg-resonance-like mechanism, valid for slightly rough surfaces, and a tangent plane (or facet) mechanism, valid for a gently undulating surface (Vesecky and Stewart, 1982). In the case of a slightly rough surface, it is assumed that the surface irregularity only slightly distorts the incident radar wave so that perturbation theory can be applied. Roughness in this context is not an absolute measurement but is expressed in terms of the wavelength of the radar's transmission signal. The Peake-Oliver "roughness criterion" (Sabins, 1978) considers a surface rough if $h > \lambda / (4.4 \sin \alpha)$, where h is the height of surface irregularities, λ is the radar wavelength, and α is the grazing angle between the sea surface and the direction of propagation of incident radar wave.

It can be seen from these criteria that a given surface will appear rougher at a shorter wavelength. An increased surface roughness results in the return signal being more diffuse. In the case of a rough surface, the rays of the scattered energy may be thought of as enclosed within a hemisphere, the centre of which is located at the point where the incident wave impinged on the surface. A rough surface acts as a diffuse (i.e., isotropic) scatterer where the scattering coefficient, σ_0 is essentially independent of the angle of incidence (MacDonald, 1980). When the root-mean-square (rms) surface roughness is considerably less than a wavelength, the surface appears "smooth" to the imaging radar. When the surface is smooth, scattering is

almost absent and reflection becomes predominant so that the reflected signal is contained in a small angular region about the angle of reflection, obeying Snell's laws of reflection. A surface of intermediate roughness reflects a portion of the incident energy and diffusely scatters the rest. In the case of a wave-laden sea surface, a mechanism known as *Bragg resonance* enhances the strength of the return signal from those waves that have a wavelength λ_s equal to $\lambda_r/(2 \cos \alpha)$, where λ_r is the wavelength of the radar transmission, and α is the depression angle of transmission. (Some aspects of the Bragg resonance mechanism are discussed in Chapter 4.) In radar imaging, near-saturated backscatter associated with maximum roughness characterizes one expression, whereas the opposite, almost entire damping of the Bragg scattering waves, often characterizes the surface slick expression.

In most situations, the basic quantity that is measured by a microwave imaging radar is the resonant wave. Various features of ocean surface dynamics modulate the energy density of these waves. These resonant waves are often modified by wind, ocean current and its gradients, surface films, and so forth. At high sea states, nonlinear effects and scattering processes other than those just mentioned may become important. Wave breaking and the associated scattering by resonant air bubbles that exist near the surface of waves under heavy sea conditions is an example. Aside from the wind- and wave-related features, most of the features observed in microwave images are presumably related to surface currents and their variations (i.e., shear). Surface currents can amplify waves by the influence of local convergence of velocity and through changes in the direction of wave propagation, leading to the focusing of wave energy. Vesecky and Stewart (1982) showed that if the resonant sea wave train—i.e., sea waves whose length is equal to $\lambda_r/(2 \cos \alpha)$ —travels with the current, its wavelength increases and the wave path tends to turn away from the current. Similarly, if the resonant sea wave train travels against the current, its wavelength decreases and the waves turn directly into the current. In the latter situation, the group velocity of the resonant wave train decreases and the resonant waves tend to pile up as they are blocked by the adverse current, reaching saturation if the blocking is strong enough. If the waves are propagating directly opposite the current, the energy density, E , of the resonant wave train is related to the energy density, E_o , of the resonant wave train in a no-current situation by this relation (Vesecky and Stewart, 1982):

$$\frac{E}{E_o} = \frac{c_o^2}{c(c + 2u)}$$

where:

u = near-surface current velocity

c = phase velocity of resonant wave train in presence of current u

c_o = phase velocity of resonant wave train in the absence of a current

This local increase in E for an adverse current (i.e., $u < 0$), and vice versa (for $u > 0$), in turn modulates σ_0 as observed by the microwave imaging radar. This variation in σ_0 of the current flow region, in comparison to the σ_0 value of the no-current region, alters the image intensity of the region where there is a surface current.

5.4. ACTIVE MICROWAVE RADAR IMAGING TECHNOLOGIES

Over the past few decades active microwave radar imaging systems have evolved into an important tool for monitoring sea surface water motion and circulation features, particularly in those parts of the globe where cloud cover presents a serious problem to optical sensors. Active microwave radar imaging systems can be broadly classified into three categories: rotating antenna radar, real aperture side-looking radar, and synthetic aperture side-looking radar. By convention, the microwave spectrum extends from 0.3–300 GHz (i.e., 1 meter to 1 millimeter in wavelength). Microwave radar was initially developed during World War II to facilitate navigation and target location using the familiar rotating antenna and circular cathode ray tube display.

It is possible to produce a good picture of the surroundings from a fixed point by rotating an antenna with a narrow beam pointing in the horizontal direction. In this type of plan position indicator (PPI) radar system, the positions of the radar “echoes” are indicated by the radial sweep on the circular display screen. A PPI radar system essentially images a continuously updated plan view map of the targets in the field of view of its rotating antenna. PPI systems are commonly employed in weather forecasting, air traffic control, and maritime navigational applications. Their resolution is rather poor for use in remote sensing for oceanographic investigations. If a rotating antenna is used on a fast-moving vehicle such as an aircraft or a spacecraft, the image will be distorted because of the forward motion of the vehicle during the antenna rotation. However, this problem is not serious on a rotating antenna system used on a relatively slow-moving vehicle such as a ship. In fact, such systems, although meant for maritime navigational applications, have been used for detection of some seawater circulation features such as plumes.

Turbulence and debris concentrated at the leading edge of the plume create sufficient relief to make the front of the plume visible on a ship's radar more than a mile away. To achieve reasonably good horizontal resolution, the antenna beam must be narrow in the horizontal (i.e., a very long antenna needs to be used). Rotating a very long antenna on

a fast-moving vehicle suffers from many practical problems. Distortion in the image resulting from the motion of the antenna-bearing vehicle is another serious handicap. For these reasons, rotating antenna systems are rarely used for remote sensing of sea surface water-motion signatures.

5.4.1. Active Microwave Imaging by the RAR Systems

Real aperture radar (RAR) systems were initially developed in the 1950s for military applications and subsequently further improved during the years of the pathbreaking Apollo missions, which culminated in the successful landing of man on the moon in 1969. After military declassification, the RAR system was developed to a high degree of sophistication to generate images of the ocean surface to monitor wave climate. Although the primary application of RAR systems for oceanographic studies was to detect ocean waves from space, the images obtained from these systems were also found to be of practical value for identification of water-motion signatures in the open seas. A side-looking microwave radar system such as RAR (Figure 5.8) produces continuous strips of imagery of the terrestrial surface areas located on one or both sides of the aircraft's flight path.

Unlike a conventional PPI system, the antenna of a side-looking radar system is not rotated to achieve scanning. Nevertheless, generation of a two-dimensional image of a large sea surface area using radar requires relative motion between the sea surface and the antenna beam. In a side-looking radar system, scanning is achieved by a fixed beam pointed to the side of a moving aircraft. The aircraft's forward motion in a straight line permits the antenna beam to scan the sea surface continuously along a straight-line path that lies on the lateral side(s) of the aircraft.

In the operation of a RAR system, a transmitter sends out a short pulse of microwave energy through an aircraft-borne long and thin antenna with a small beam width, β_a , in the along-track direction and a large beam width, β_c , in the vertical plane normal to the flight direction (see Figure 5.9).

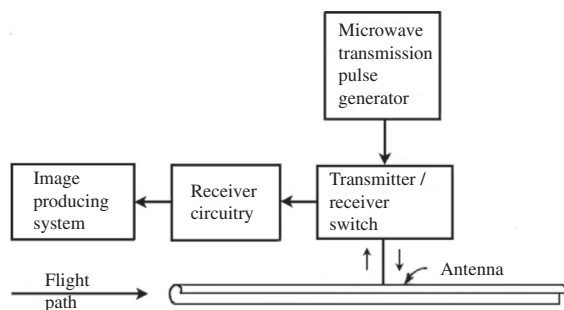


FIGURE 5.8 Schematic diagram showing the operation of a real aperture side-looking microwave radar system.

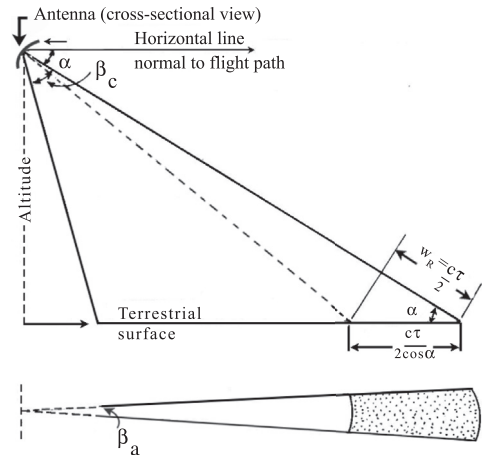


FIGURE 5.9 View of the beam orientation of a real aperture radar system. (Top) Side view in a vertical plane normal to the flight direction. Relationship between slant-range resolution, W_R , and ground-range resolution, W_C , in the cross-track direction is shown. (Bottom) Plan view as projected on the sea surface.

The beam is pointed to the side of the flight track through a large elevation angle. The beam width, β_a , determines the resolution in the flight direction. The pulse width, τ , determines the resolution normal to the flight path (i.e., range resolution). As the microwave energy impinges on the terrain surface, it gets scattered in different directions depending on the nature of the sea surface. The portion of the radiation backscattered in the direction of the radar is intercepted by the same antenna. The electrical signal so induced at the antenna is sent out to a sensitive radio receiver. The signal is amplified by the receiver in such a way that amplification increases with time so as to compensate for the decreasing echo strength at successively greater ranges. Introduction of such a time-varying gain (TVG) during signal conditioning ensures that, irrespective of range differences of various "targets" from the antenna, a signal is created for which the amplitude depends on the magnitude of the original radiation backscattered at any instant from a strip of terrain normal to the flight direction. As the forward motion of the aircraft carries the antenna forward relative to the sea surface, the footprint of the microwave beam on the sea surface automatically moves to new positions so that succeeding pulses sense the microwave reflectivity of the adjacent strips of the sea surface, which is oriented perpendicular to the flight direction. The signals received from adjacent terrain strips are then used to generate a two-dimensional image of the terrain parallel to the flight direction.

Various techniques have been used for the generation of images of the sea surface from the received signal. In the conventional method, the detected signal is made to control the brightness of a linearly moving spot of light on the face of a cathode ray tube (CRT). The speed of the moving spot of

light so generated on the CRT covers the entire ground range normal to the flight path, embraced by the antenna beam. This intensity-modulated signal, displayed in a single line in the same position on the face of the CRT for each pulse transmitted, is focused by a lens system onto a single line on a photographic film that moves in front of the CRT in a direction transverse to the single-line display. Brightness of various parts of the line depends on the strength of the echo received from various points along the strip scanned on the sea surface. The forward movement of the aircraft causes a different strip of sea surface to be illuminated by the radar all the time. The motion of the film is in synchrony with the motion of the aircraft. This permits recording of the image of the adjacent sea surface strips on adjacent filmstrips. The length of the sea surface strip illuminated by the radar beam is usually 100 km or more. The film, when chemically processed, provides a map of the texture corresponding to the microwave reflectivity of the terrestrial surface swept by the antenna beam. The texture features are then interpreted to evolve useful information about the sea surface features. The interpreter must, however, take into account the possible distortions in the image, introduced by various factors, before attributing a physical meaning to the observed features in the image. The possible causes for distortions in the image include attitude or lateral changes of the aircraft, which is caused by turbulence in the atmosphere; yaw, pitch, or roll motions of the aircraft; or lack of synchrony of the drive systems in the imaging electronics with the speed of the aircraft.

In some modern systems, the detected output from the receiver is fed to a CRT or digital scan converter. When the scan converter is full, the signal is displayed in TV format on a video display monitor. Compensation for aircraft speed may be achieved in the scan converter by adjusting the scan rate (Ulaby et al., 1982). Images corresponding to each successive screenful of data are either photographed by a camera that is synchronized with the display or recorded on an onboard videotape that can be later played back on the ground. The latter method helps overcome some of the difficulties associated with setting up the contrast and brightness controls for the TV monitor during flight. Some RAR systems use telemetry for transmission of the detected signal to a ground station.

The quality of an imaging radar system is judged by its resolving power (also termed *resolution*) and is taken as its ability to distinguish between closely spaced targets. In practice, the resolution of an imaging radar system is the size of the cell area as projected on the ground, resulting from the impinging of a single radar pulse. This ground resolution cell area is conventionally called *pulse rectangle of ground-resolvable area*, although it is not a true rectangle (see Figure 5.10). The integrated reflectance from all the targets within the ground resolution cell area at any given instant in time is sensed by the radar receiver as

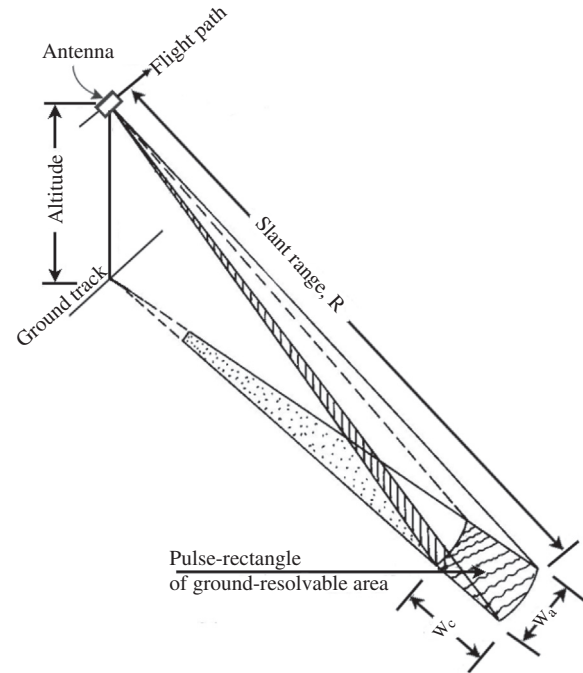


FIGURE 5.10 Schematic diagram showing pulse-rectangle of ground-resolvable area of an imaging real aperture radar system.

though they were all located at the center of the rectangle. This means that two or more targets located within this ground resolution cell will be seen by the radar as a single target. Thus, an important task of the system designer is to minimize the ground resolution cell area so that sea surface features can be better resolved. When the composite reflectance value from a given ground resolution cell differs from those in adjacent cells, the radar receiver is said to be able to *discriminate between adjacent targets*.

The dimensions of the ground resolution cell of a RAR system are determined by a combination of resolutions in the along-track and cross-track directions. These dimensions are different in the two orthogonal coordinates of the image. Spatial resolution, W_a , in the azimuth direction (i.e., in the flight direction) is determined by the angular width of the sea surface strip, which is illuminated by the radar beam at the range of interest. W_a is usually taken to be the arc length of the antenna at the range of interest; i.e., $W_a = \beta_a R$, where R is the slant distance from the antenna aperture to a given scattering target, and β_a is the 3-dB beam width, in radians, in the far field of the antenna in the along-track direction. According to the well-known Rayleigh criterion, $\beta = (\lambda / L)$ radians, where λ is the transmission wavelength, and L is the antenna length. Usually it is assumed that the antenna is focused to infinity (i.e., aperture with uniform phase), and the beam width is defined in the far zone. With very large values of L , due consideration must be given to the far-zone condition of the antenna. The far-zone distance R_{fc} is given by (Tomiyasu, 1978) $R_{fc} = (2L^2) / \lambda$.

The antenna beam width, β_a , is given by $\beta_a = (\lambda / L_a)$, where L_a is the length of the antenna in the along-track direction. By taking the relationship $W_a = \beta_a R$ into account, $W_a = (\lambda \times R) / L_a$. It can be seen from the preceding expression that, for a given transmission wavelength, resolution in the along-track direction can be enhanced by increasing the antenna length in the along-track direction. For this reason, a long antenna is used for imaging by the RAR system. It is also seen that, for a given antenna length L_a and a given transmission wavelength λ , the along-track resolution deteriorates as the antenna beam “fans out” with increasing range from the aircraft.

Spatial resolution, W_R , in the slant range direction (i.e., in the direction of propagation of the transmitted pulse from the antenna to a given target area) is determined by the transmitted pulse duration, τ , and is given by the expression $W_R = (c\tau)/2$, where c is the speed of electromagnetic radiation in the medium of travel. If the receiver bandwidth, B , of the radar system is matched to τ , then $B = (1/\tau)$ so that $W_R = c/(2B)$. The slant-range resolution ($c\tau/2$) is the difference in range of two points of which the reflected signals differ in arrival time by τ . Thus, the cross-track resolution (i.e., range resolution in terms of the horizontal cross-track distance on the sea surface) is given by $W_c = \frac{c\tau}{2\cos\alpha}$, where α is the depression angle (i.e., the angle between the horizontal plane on the sea surface and the straight line connecting the antenna aperture to a given target area). Thus, as the depression angle approaches 90° , the cross-track resolution approaches infinity. For this reason, vertically downward-looking radars give poor cross-track resolution.

Cross-track resolution, however, improves as depression angle is decreased. For this reason, imaging radars are oriented to “look” to the side of the flight path rather than vertically downward. The significance of W_c is that only those targets separated by a distance more than W_c in the cross-track direction can be distinguished unambiguously by the radar as separate targets. Those targets separated by a distance less than W_c will be recognized by the radar as a single target. Better cross-track resolution means that the value of W_c is minimal. It can be seen from the expression $W_c = \frac{c\tau}{2\cos\alpha}$ that W_c can be enhanced (i.e., minimized) either by decreasing the depression angle α or by shortening the pulse length τ . Shortening τ reduces the amount of energy in each pulse transmitted from the antenna, which, in turn, results in reduced strength of the return signal. To meet the S/N ratio and target detection requirements, a high average radiated power can be obtained by a high transmit pulse duty cycle. These requirements on the transmitter are satisfied by transmission of a linearly swept frequency-modulated (FM) long pulse known as a *chirp pulse* (see chapter 12 for *chirp waveform*). The chirp pulse is usually generated by

transforming short wideband pulses into long pulses with the same swept bandwidth utilizing a frequency-dispersive delay line. These long pulses are then amplified by a high-power amplifier, passed through a circulator (switch), and then radiated by the radar antenna. The received signal passes through the same circulator, is amplified, and then is pulse-compressed. The pulse-compression circuit can use a delay line and a summing circuit, which converts the wideband chirp signal into a short pulse signal with the same bandwidth (see chapter 12 for details). The drawback of shortening τ is thus resolved by transmission of a long chirp pulse and then shortening the apparent pulse length of the return signal by an ingenious signal-conditioning technique, at the same time achieving enhanced signal strength.

It has been observed that decreasing the value of α results in an enhancement of W_c . However, this would also mean an increased range from the radar to a given target area. At large ranges, the spatial resolution in the along-track direction is rather poor (see Figure 5.11). This calls for a compromise in the design of an imaging radar system. Improved sea surface area coverage and good spatial resolution are achieved by careful design of the radar system. It can be seen from the relation $W_c = \frac{c\tau}{2\cos\alpha}$ that the cross-track resolution does not depend on beam width. However, a large beam width, β_v , in a vertical plane in the cross-track direction will provide a large coverage by the beam in the cross-track direction. This is achieved by configuring the antenna dimension in the vertical direction, L_v , to be small. In this case, $\beta_v = (\lambda/L_v)$.

The requirements of a narrow beam in the along-track direction (for better azimuth resolution) and a wide beam in the cross-track direction (for greater area coverage) are together met by the use of a long semicylindrical reflector antenna of small diameter fed by a dipole array. The antennae in some instances were as long as 15 meters and were fixed parallel to the fuselage of the aircraft (Ulaby et al., 1981). Such an antenna looks sideways with a fan beam that is wide in a vertical plane and narrow in

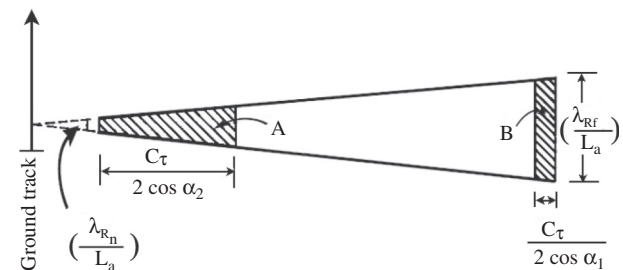


FIGURE 5.11 Schematic diagram showing dependence of along-track and cross-track resolution cell dimensions on horizontal distance from ground track. A indicates spatial resolution cell area at short slant range R_n and large depression angle α_2 . Likewise, B indicates spatial resolution cell area at far slant range R_f and small depression angle α_1 .

a horizontal plane. Because the beam is wide vertically, its projection on the ground contains several slices, in a linear array, the length of which in the cross-track direction is given by $\frac{c\tau}{2\cos\alpha}$ and in the along-track direction by $\frac{\lambda R}{L_a}$.

Generation of good imagery requires careful data acquisition and processing procedures. Despite transmission of a narrow pulse, the received signal is extended in time because of the long beam length projected on the sea surface in a direction normal to the flight path. The first part of the received echo has come from the *nearest* part of the illuminated area at range R_n at a time t_n after transmission. Reception continues until the echo from the *farthest* illuminated point at range R_f has arrived at time t_f after transmission. The number of pulse length τ that can be fitted between t_n and t_f is the number of independent measures of W_c that can be obtained across the swath. The depression angle α_f corresponding to the farthest illuminated point is a minimum, and the depression angle α_n corresponding to the nearest illuminated point is a maximum. This results in an increasing degradation of W_c from the farthest to the nearest illuminated points.

If imagery obtained from radar is to be realistic, it is necessary that the pulse repetition rate vary inversely with the range of operation, because all return signals from an outgoing pulse must be received before sending out another pulse. Such a scheme avoids simultaneous reception of returns from multiple scene elements (Lowe, 1980).

Another problem inherent in an imaging radar system is geometrical distortion of image in the cross-track direction. This arises because the radar measures time delays, and therefore areas nearer to the flight path appear compressed relative to the areas farther to the flight path, unless the distortion is corrected by digital processing techniques (Elachi, 1980). All these factors require that the designer make some compromise among performance parameters such as range of operation, depression angle, swath width, and spatial resolution.

5.4.2. Active Microwave Imaging by SAR Systems

It has been indicated in the discussion on RAR that, for a given antenna length and a given transmission wavelength, the along-track resolution deteriorates as the antenna beam fans out with increasing range from the radar. The optimum RAR configuration, to achieve good range and azimuth resolutions, is that of high-frequency radar carried on a low-flying aircraft. At long ranges, as in the case of satellite-borne radar, an antenna of a few kilometers long will be necessary to achieve along-track resolution of a few tens of meters. Such an antenna is impractical for a spacecraft. The impracticability of attaining good azimuth

resolution from conventional radar flying at high altitudes has been resolved with the application of an ingenious technology known as *synthetic aperture radar* (SAR).

SAR is a coherent active microwave imaging device (i.e., one in which both transmitter and receiver are phase-referenced to a stable master oscillator). In remote sensing it is used for mapping the scattering properties of a large surface area in the respective wavelength domain. Many physical and geometric parameters of the imaged scene contribute to the gray value of a SAR image pixel. Scene inversion suffers from this high ambiguity and therefore requires SAR data taken at a different wavelength, polarization, time, incidence angle, and so on. SAR was initially developed in support of various lunar mission programs in order to obtain a microwave photograph of the lunar surface with fine resolution. Microwave imaging systems were necessary to obtain images during both day and night. To realize an along-track resolution that is significantly finer than that dictated by the angular beam width of the radar antenna, the SAR system employed coherent radar in conjunction with data storage and processing of the radar signal Doppler spectrum. The data collected during the observation time were processed to synthesize a large-antenna aperture.

The radar data from the lunar mission were recorded on photographic film and were returned to Earth for processing. A combination of optical and digital processing technologies was applied to the scientific interpretation of the data. Because the return signal level was strongly influenced by the degree of flatness of the scattering surface, excellent imagery of the lunar surface could be obtained. The success of the SAR system designed for the lunar mission programs showed considerable promise for its application to imaging of terrestrial (both land and ocean) surfaces. Subsequently, aircraft-mounted SAR systems were designed and field-tested. Airborne SAR systems proved their worth in imaging some oceanic features such as waves and water-motion trajectories.

A space-borne or airborne SAR illuminates the Earth's surface in a side-looking fashion. Whereas the sensor is moving along its assumed straight path at an altitude H above some reference plane, it transmits microwave pulses into the antenna's illumination footprint at the rate of the *pulse repetition frequency* (PRF) and receives the echoes of each pulse scattered back from Earth. The SAR receiver detects the stream of echoes coherently and separates it into individual echoes, each corresponding to a transmitted pulse. For processing, the echoes are preferably arranged side by side as a 2D matrix, with coordinates of *two-way signal delay time* and *pulse number*. The pulse number relates to the satellite position along its flight path, and the delay time relates to slant range. Typical pulse-carrier wavelengths are approximately 3 cm (X-band), 6 cm (C-band), 9 cm (S-band), and 24 cm (L-band). In addition, 64 cm (P-band) might be used in the

future. PRFs are in the range of 1–10 kHz. The ensemble of scatterers is assumed to be temporarily stationary and to reside in the far field of the SAR antenna. The antenna look direction will be perpendicular to the flight path, although this is never strictly true in real systems.

Thus, in SAR, a coherent phase history of the pulsed return signal is generated, and through a signal processing technique, extremely high resolution in the azimuth direction is attained without the use of a physically large antenna. In effect, a large aperture antenna is thus synthesized. A SAR achieves its characteristically fine along-track resolution by coherently summing the signals received during a period of time on the order of a second and correcting the phase of these signals so as to simulate the signal that would have been received by a single antenna having a length equal to the distance traveled by the SAR during the integration period. For stationary surfaces, this aperture synthesis technique is capable of producing an along-track resolution equal to half of the actual SAR antenna length (see Figure 5.12). However, for moving surfaces such as the ocean, the phase of the received signal fluctuates randomly during the integration time, thereby severely limiting the theoretically achievable along-track resolution.

Spatial resolution obtainable from a SAR in the cross-track direction is the same as that obtainable from a RAR in the cross-track direction. Because SAR generally operates from a very large height above the sea surface, it is necessary that the transmitted pulse be sufficiently strong. To achieve fine cross-track resolution, it is also necessary that the effective pulse width of the transmission signal be very small. However, higher power cannot be pumped into a short pulse. These two conflicting requirements of narrow pulse width and high power are met by transmission of a chirp pulse and then by ingeniously processing the received signal to make the pulse length of the return signal effectively short.

The SAR technology originated with an observation by Carl Wiley in 1951 that a radar beam oriented obliquely to

the radar platform velocity vector will receive signals that have frequencies different from the radar's carrier frequency as a consequence of the Doppler effect. He noted that the Doppler frequency spread was related to the width of the antenna beams and that the desired narrow beam can be synthesized by appropriate signal processing. Wiley also noted that the narrowest angular beam would occur "broadside" to the platform velocity. Taking a cue from these observations, the ensuing years witnessed vigorous research activities in the realm of hardware and signal-processing technologies, thus culminating in the development of operational SAR systems. The SAR system is a very complex device and therefore only a bird's-eye view of the basic principles is provided here.

SAR is a phase-coherent sensor that repetitively transmits high-power pulses and detects the backscattered return signals. The received return signals are processed coherently to produce high resolution two-dimensional images of the mapped areas. The raw data acquired by coherent radar resemble a hologram rather than an image and hence require a considerable amount of signal processing for image formation (or "focusing"). The SAR is essentially composed of a high-power signal transmitter, a side-looking antenna moving at the same altitude with a constant velocity, a circulator, and a phase-coherent receiver. As in the case of RAR, the antenna of a SAR system is time-shared between the transmitter and the receiver by utilizing a circulator (switch). The typical SAR transmitter is designed to overcome the limitations of peak power in components and to satisfy stringent azimuth and range resolution requirements. High spatial resolution in the along-track direction (azimuth) is achieved by an effectively very long antenna synthesized from a small antenna. In fact, the heart of SAR technology lies in the synthesis of a very long antenna, thereby effectively generating a beam that has a very small width β_a in the far field of the antenna in the along-track direction. In achieving this goal, the really big difference between SAR systems and other radar systems lies in the signal processor. In short, in the oceanographic context, SAR maps the sea surface to a fine resolution with a fixed side-looking antenna using the artifice of simulating a large antenna by moving a comparatively smaller one. Range resolution is achieved in the standard manner with short pulses, but azimuthal resolution relies on mapping Doppler shifts into positions on the sea surface. This technique is briefly addressed in the following section.

5.4.2.1. Synthesis of Long Antenna from Small Antenna

In the synthesized antenna array concept, a very long antenna is constructed in principle essentially by an array of numerous small elemental radiators placed sufficiently

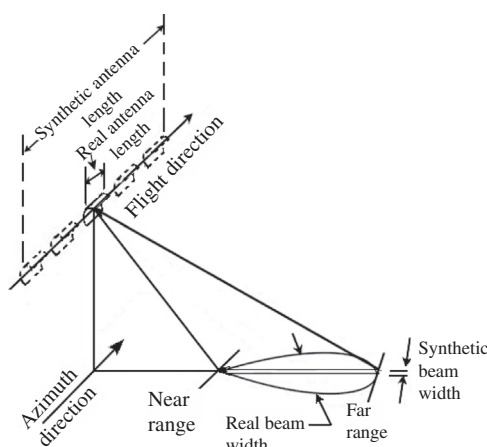


FIGURE 5.12 Schematic diagram showing the method of deriving narrow synthetic beam width for SAR from a broader real beam width.

close together to prevent grating lobes in the angular directions of interest and properly phased to focus the aperture at the midarray range, R_o to the target. Instead of exciting all elements of this hypothetical array simultaneously, each element of the long linear array is excited in sequence so that an orderly, coherent phase relationship is maintained.

The array mentioned here is only a concept, implemented in practice, using small moving radar. The ingenious scheme used in the SAR imaging system is that a hypothetical long linear array of numerous radiating elements is constructed effectively by a simple physical radiator (antenna) moving in a straight line at a constant velocity, V , with the radiator transmitting pulses periodically as it is laterally displaced by a proper amount. In this manner, the equivalent of a very long linear antenna array with synthetic aperture length, L_{sa} , is synthesized from a number of small elements equal in number to the pulses transmitted and integrated coherently. This synthesized antenna array is called a *synthetic aperture radar*. For simplicity we shall consider only a few positions of the radar antenna on the airborne vehicle with respect to a target, T , on the sea surface. In actuality there are numerous hypothetical radiators between the extreme positions, radiating at spatial intervals satisfying certain conditions discussed later. The total possible length of the synthetic aperture, L_{sa} for a given target position is the distance between points where the forward edge of the beam first intercepts the target (say, position A) and the point where the aft edge of the beam is just leaving the target (say, position C). According to the “close-target separability criterion,” the azimuth resolution, W_a , obtainable from a focused long array, is given by (Tomiyasu, 1978):

$$W_a = \frac{\lambda R_o}{2L_{sa}} \quad (5.1)$$

In this expression, R_o is the midarray range to the target, and λ is the radar transmission wavelength. The radar’s radian viewing angle, θ_R , relative to the target is given by:

$$\theta_R = \frac{L_{sa}}{R_o} \quad (5.2)$$

θ_R is also the one-way radar antenna beam width that can provide a dwell time T_d . The real aperture radar antenna length L_R , which can produce a beam width θ_R , is given by:

$$L_R = \frac{\lambda}{\theta_R} \quad (5.3)$$

From relations (5.2) and (5.3),

$$\lambda R_o = L_R \times L_{sa}$$

Substituting for λR_o in (5.1) we get $W_a = \frac{L_R}{2}$.

Thus, if the antenna is fixed to a moving vehicle, the finest possible azimuth resolution obtainable from SAR is just half the length of the real aperture. This azimuth resolution is independent of range and also independent of wavelength. The synthetic beam is narrower and also of equal width, irrespective of range. The reason that the synthetic beam is independent of range is that L_{sa} is itself directly proportional to the range, because of which a larger range results in a larger aperture. The reason it is independent of wavelength is that for longer wavelength, L_{sa} is also proportionately longer. The net result is that the azimuth resolution remains the same because the equivalent synthetic beam width remains the same (Ulaby et al., 1982).

The result also shows that very fine resolution images can, in principle, be produced with a small radar antenna. This welcome result is contradictory to that obtained for real aperture radar, where a large antenna is required to obtain fine azimuth resolution. Although it is desirable to use a very small radar antenna so as to attain the theoretically achievable fine azimuth resolution in SAR imagery, the radar antennas used in practice are not very small. For example, the Seasat-A SAR antenna system had dimensions of $10.74 \text{ m} \times 2.16 \text{ m}$ (Jordan, 1980). The deployed antenna was configured to fly with the long dimension along the spacecraft velocity vector and boresighted at an angle of 20.5° from the nadir direction in elevation and 90° from the nominal spacecraft velocity vector. The reason for the use of a relatively large antenna in SAR systems is that the reduction in size of the antenna length, L_R , is limited by the requirement to generate a sufficiently powerful signal. Resolution of SAR can be made finer than $(L_R/2)$ with the use of a scanning antenna. The scanning motion, however, will result in gaps in coverage along the flight path (Ulaby et al., 1982). This is undesirable for a radar system, which is meant for imaging a large area along its flight path. For this reason fixed antennas are used with operational SAR systems.

In the case of Seasat-A SAR, the data were collected at a rate of approximately 10^6 resolution cells per sec. Such a vast amount of information could not be stored onboard the satellite and was, therefore, telemetered to five ground stations, located in the United States (California, Florida, and Alaska), the United Kingdom, and Canada. SAR images could be obtained only when the satellite was in the horizon of one of these stations.

5.4.2.2. Enhancement of Azimuth Resolution

It has been observed that fine-resolution images can, in principle, be produced by the small radar antenna of a SAR system. In practice, high spatial resolution in the azimuth is achieved by signal processing the amplitude and total phase history of the signals reflected by the targets and collected by the SAR receiver for the dwell time period T_D . The

interval during which the target area is illuminated is called the *integration time* or *dwelt time*, T_D . It may be noted that the distance traversed by the radar platform while illuminating the target T during the dwell time period T_D is the synthetic aperture length, and this dimension is exactly the linear beam width of the radar antenna beam at range R_0 (R_0 is the midarray range to the target). For an isolated target, the phase history during the dwell time follows a quadratic phase function given by (Tomiyasu, 1978):

$$\phi(x) = \frac{(x - x_o)^2}{\lambda R_o} \text{ wave-lengths} \quad (5.4)$$

In this expression, the terms have the following meanings: $\phi(x)$ is the two-way phase change as a function of the straight distance of the radar relative to the midpoint of the synthetic aperture array; x is the position of the radar platform relative to the midpoint of the synthetic aperture array; R_o is the nearest range of the radar to a given target; x_o is the radar position in the synthetic aperture array corresponding to R_o ; and λ is the radar transmission wave length. The two-way phase change as a function of time, $\phi(t)$, is obtained by converting the position parameter x to time t . Accordingly,

$$\phi(t) = \frac{v^2(t - t_o)^2}{\lambda R_o} \text{ wavelengths} \quad (5.5)$$

where v is the constant velocity of radar platform; t is the time variable corresponding to position x . The two-way Doppler frequency, f_D , is the time derivative of $\phi(t)$. Accordingly,

$$f_D = \frac{d\phi}{dt} = \frac{2v^2(t - t_o)}{\lambda R_o} \quad (5.6)$$

This relation indicates that the Doppler frequency changes linearly with time. In a SAR system, the phase history is recorded over a time interval from $(-T_D/2)$ to $(+T_D/2)$ in which T_D is the coherent integration time for a “single-look” SAR system. T_D is also equal to the target illumination time, popularly known as the *dwelt time*. The SAR processor expects the quadratic phase history given by the relation in Equation 5.5, and by matched filtering it positions the facet at zero Doppler. In practice, the signal amplitude and phase history are recorded on film or memory after phase-coherent addition of the received signal with a reference signal. When two signals are in phase, a higher combined level is obtained than when out of phase. Targets that cause zero Doppler shift lie on a plane strip that is oriented at right angles to the radar platform velocity vector. This plane must lie at the center of the broadside beam. Thus, measurement of Doppler shift permits processing the return signal amplitude, for sea surface imaging purposes, from only those targets that lie on a thin strip of

the sea surface and that lie at the center of the wide area illuminated by the radar beam at a given instant. This process permits us to obtain fine spatial resolution in the azimuth. From measurement of total Doppler shift during the dwell time, it is possible to calculate the azimuth resolution achieved by a SAR system. Referring to the relation in Equation 5.6, in the limiting case, $(t - t_o) = T_D / 2$ so that:

$$\pm f_D = \frac{v^2 T_D}{\lambda R_o} \quad (5.7)$$

The total Doppler frequency change during the target illumination period is $2f_D$, so that:

$$f_{D(\text{total})} = \frac{2v^2 T_D}{\lambda R_o} \quad (5.8)$$

The time that the target is illuminated by the radar beam, i.e., dwell time, is given by $T_D = \frac{L_{sa}}{v}$, so that $L_{sa} = vT_D$. Substituting this value of L_{sa} in Equation 5.1, we get $W_a = \frac{\lambda R_o}{2vT_D}$, so that:

$$\lambda R_o = 2W_a v T_D \quad (5.9)$$

Substituting the value of λR_o in Equation 5.8, we get

$$f_{D(\text{total})} = \frac{2v^2 T_D}{2W_a v T_D} = \frac{v}{W_a}.$$

Thus, azimuth resolution:

$$W_a = \frac{v}{f_{D(\text{total})}} \quad (5.10)$$

For Seasat SAR, $v \approx 7.2$ km/s, and $T_D \approx 2.3$ s. This yielded a synthesized aperture length $L_{sa} \approx 17$ km. The single-look azimuth resolution obtainable from Seasat SAR was approximately 6.6 m. In practice, four azimuth resolution cells, or “looks,” are incoherently averaged with a resulting “four-look” azimuth resolution of approximately 25 m, which matches its cross-track resolution of ≈ 25 m.

It has been seen that the theoretically achievable azimuth resolution of a SAR system is equal to one-half the antenna length in the flight direction. However, to attain this resolution in practice and to maintain continuity of the image in the azimuth direction, the radar platform displacement must not exceed one-half the antenna length L_R in the azimuth direction between successive transmit pulses. To avoid azimuth ambiguity in the SAR operation, this geometric constraint on the pulse-to-pulse displacement of the antenna beam is a particularly important feature. This means that the pulse repetition frequency (PRF) must be at least $\frac{v}{(L_R/2)}$. Thus, $PRF_{(Low)} = \frac{2v}{L_R}$. The

upper limit of the PRF is governed by the requirement that the return signals arising from two successive transmitted pulses must not arrive at the receiver simultaneously. If the PRF is so high that the pulses overlap and simultaneous reception takes place, there will be ambiguity in the response. The upper limit of PRF is given by $PRF_{(upper)} = \frac{1}{2\tau + 2(R_f - R_n)/c}$, in which τ is the transmission pulse length; R_f is the far range; R_n is the near range; and c is the velocity of electromagnetic radiation in the medium of travel. These criteria for lower and upper limits of PRF ignore, for simplicity, the effect of the curvatures of the Earth and the satellite orbit. However, these lower and upper limits are severe constraints on the design of practical SARs.

To obtain the theoretically achievable resolution of SAR, the method employed is to transmit pulses at a suitable repetition frequency. Because the radar is in constant motion along its flight path while transmission takes place, any given target point in the field of view of the radar is illuminated several times during the dwell time. The number of times a given target point is illuminated in a given pass depends on the PRF. Consequently, in a given pass, return signals from any given target point are received at the radar receiver many times during the dwell time. The number of times the return signals from any given target point are received in a given pass again depends on the PRF. The returns from the entire target points at all ranges in the field of view of the radar are stored in memory.

Signal processing commences after collection of signals for specified time duration, often a specified number of dwell times. Because any given target point is illuminated by the successive transmission pulses at progressively changing phases with respect to their phase at the center of the radar aperture, the phases of the successive return signals from any given target point progressively vary from one extreme to the other, with a phase distribution symmetrical about the center of the radar aperture. If each of the received signals from a given target point is correlated with a reference signal appropriate for its phase history and then added, only those signals that arrived from the point of closest approach to the radar will add constructively. All the other signals received from this target point add destructively, depending on the phase geometry. This governs the effective beam width and, therefore, the azimuth resolution. Thus, by appropriate data processing of the successive return signals from a given target point, the effect of using a very wide real aperture antenna is achieved. Depending on the PRF, some side lobes may be generated in the addition process. These side lobes are generally much smaller in size than the central peak of the overall summation of the signals across the aperture.

In the preceding discussion, returns from only a single target point (a resolution cell) have been considered for simplicity in understanding the basic operation. In actuality, returns from all target points (resolution cells) that are swept by the radar beams are received over a dwell time and recorded in the receiver memory as the radar passes over the target points. Subsequently, data processing as applied in the case of a single target point is successively applied to all target points so that a high-resolution image of the sea surface strips is generated without any discontinuities. To perform this data processing, the location of each target point and its phase history must be known to the processor. Location is determined from the range, which in turn is determined from the pulse travel time. The phase history of a given target point is determined from the Doppler history of the particular target position for which the back-scattering cross-section is being evaluated. The steady motion of the radar in the azimuth direction produces a Doppler shift in the frequency of the returned signal. As the radar approaches a target point, the contribution of that point to the reflected signal is first at a higher frequency than the transmitted signal and then gradually reduces in a linear way until it is less than the transmitted signal when the radar has passed by. At any given time for a given range, the contributions from each target point along the azimuth at that range can be identified uniquely by its Doppler-shifted frequency. This enables the phase history of each target point to be determined and the summation of different contributions from different target points to be performed so as to achieve fine azimuth resolution.

For high-precision SAR processing, determination of the absolute Doppler centroid is essential. The Doppler frequency associated with a target located at the azimuth beam center line is called the *Doppler centroid*. Due to the pulsed nature of the SAR system, sampling of the target spectrum takes place discretely at the PRF. This means that the interval of unambiguous Doppler spectrum is limited to the PRF. These aspects have been addressed by Li et al. (1983). Doppler centroid error leads to significant degradation of the S/N ratio and to an azimuth shift of the pixel location. Because the antenna ephemeris data and antenna altitude data are not sufficiently precise to provide accurate Doppler centroid estimation, the Doppler information has to be derived by analysis of the coherent radar return signal. An essential requirement to be satisfied by such a Doppler centroid tracker algorithm is that it should be able to follow the Doppler frequency variation, even across the PRF band boundaries. In some cases, an accurate Doppler centroid estimate can be extracted from the SAR data through a clutter-lock process. However, most of the clutter-lock methods have been optimized for the case wherein the target is strictly homogeneous. The majority of real targets

are quasi-homogeneous, wherein the backscatter coefficient varies as a function of position. Improved algorithms continue to be developed for further enhanced estimation of Doppler centroid. Three such popular methods are the ΔE method, the correlation Doppler estimator, and the sign Doppler estimator.

Because the space-borne SAR systems operate in the microwave (centimeter-to-decimeter wavelength) regime of the electromagnetic spectrum and provide their own illumination, they can acquire information globally and almost independently of meteorological conditions and sun illumination. They are, therefore, most suitable for operational monitoring tasks. There is little attenuation of the radar signal by the intervening atmosphere. Once the SAR's radiation reaches the ocean surface, the electromagnetic properties of which are quite homogeneous, penetration is limited to about a tenth of the wavelength of the radar. Thus, SAR backscatter from the ocean results from sea surface roughness elements having a wavelength on the order of that of the radar. The side-looking imaging geometry, pulse compression techniques, and the synthetic aperture concept are employed to achieve geometric resolutions in the order of some meters to tens of meters with physical antennas of modest size. The price to be paid for such favorable performance is high transmit power, a considerable amount of signal processing, and—compared to optical imagery—“unconventional” imaging geometry.

The commonly used SAR imaging geometry is known as (continuous) *stripmap mode*. Two other SAR mapping modes are of interest: ScanSAR and spotlight mode (Bamler and Hartl, 1998). The SAR integration time, i.e., the duration a scatterer is illuminated by the radar, determines the azimuth (x -) resolution of the final image. In the stripmap mode configuration, the integration time is given by the azimuth extent of the antenna pattern. In ScanSAR mode (Ahmed et al., 1990; Bamler and Eineder, 1996; Cumming et al., 1997; Monti Guarnieri and Prati, 1996; Monti Guarnieri et al., 1994; Moore et al., 1981; Moreira et al., 1996; and Tomiyasu, 1981) the integration time is deliberately shortened by operating the SAR in a burst mode, where it periodically transmits bunches of pulses (bursts). In the time between bursts, the look angle of the antenna beam is changed to illuminate a swath parallel to the previous one. Following this routine, the SAR sweeps its beam in a stepped manner from swath to swath before it returns to the first-look direction. Hence, a ScanSAR system images several swaths temporarily interleaved at about the same time. During processing these swaths can be stitched together to give a total swath of up to 500 km width. The consequence of the enormous coverage is the reduced resolution due to the burst-mode operation.

The complementary approach is adopted by spotlight SAR (Carrara et al., 1995; Di Cenco, 1988; Gough and Hawkins, 1997; Munson et al., 1983; and Walker, 1980).

Here the antenna is continuously steered toward a certain patch on the ground in order to keep it in view over a longer time. The increased integration time results in a higher azimuth resolution at the expense of coverage: A spotlight SAR can only image selected and isolated patches, whereas stripmap mode and ScanSAR map strips of theoretically unlimited length.

5.4.2.3. Sources of Errors

Because SAR is a phase-coherent system, generation of high-quality radar images requires that it generate accurate phase histories. The principal sources of phase errors are imperfections such as unsteady radar platform velocity, motion of target points, electromagnetic path-length fluctuations, Earth rotation effects, and instabilities in the electronic circuitry. Another cause of degradation in image quality arises from speckle. Because measurement of phase histories of returned signals plays a very important role in signal processing, phase stability is an exceedingly important factor in a SAR system. The primary oscillator that provides the signal for the transmitter as well as the reference for the receiver must be very stable. The timing of the transmit pulses must be very precise with respect to the primary oscillator.

In high-resolution SAR systems, it is important to know the precise position of the antenna during the integration time. To achieve coherent integration of the successive received pulses, which is the essence of a SAR system, it is necessary that phase errors resulting from spurious antenna-motion error (i.e., the error between the actual flight path and the nominal one) are compensated. For a SAR system mounted on aircraft, motion errors are considerably large due to atmospheric turbulence and aircraft properties. Typically the position of the antenna is calculated from the navigation data of the inertial navigation system on board the airplane.

A number of factors can cause errors in the calculated position. For example, an error can occur due to vibration of the antenna lever arm. Any such residual motion exceeding a small fraction of the carrier wavelength will cause considerable phase corruption, thereby rendering the resulting image worthless. By optimal mechanical design, the residual motions may be reduced to a certain extent. Another method is to actually measure the high-frequency residual motions and then compensate for the errors. In addition to these mechanical means, signal processing methods can also be used to estimate the residual motion and subsequently to remove its phase corruption from the radar signal.

Other motion errors arise from yaw, pitch, and roll motions of the antenna platform. If motion errors of the antenna are known, motion compensation can be realized by adjusting the PRF, applying a range-dependent phase shift to each received pulse, and delaying it. By adjusting

the PRF, motion errors arising from the forward velocity variations of the antenna can be compensated.

By adjusting the range and phase delay, it is possible to compensate for the antenna displacement in the line-of-sight direction. Moreira (1990) has reported a method to extract the displacement in the line-of-sight direction, antenna velocity, and the yaw-and-drift angle from the SAR raw data. This method is based on the analysis of the azimuth spectrum of the raw data. The primary condition to implement this method is the use of a wide-azimuth antenna beam. This method for real-time motion compensation seeks to extract all the necessary motion of the aircraft from the radar backscatter signal. Hence, an inertial navigation system becomes unnecessary for several applications. The motion-compensation parameters for real-time motion-error correction are range delay, range-dependent phase shift, and PRF. The motions of the aircraft extracted by this method are displacement in the line-of-sight direction, antenna yaw-and-drift angles, and forward velocity. Extraction of the motion errors of the aircraft is based on two schemes. The first scheme analyzes only the ground reflectivity part of the azimuth spectrum and is known as the *reflectivity displacement method* (RDM). The second scheme analyzes only the antenna pattern part of the azimuth spectrum and is known as the *spectrum centroid method* (SCM).

For satellite-borne SAR, the satellite orbit planes are referenced to space, and sea surface targets have an apparent motion at Earth rotational rates. Such apparent motions cause various errors such as image shifts and azimuth defocus. These errors are greatest when the satellite is crossing the equator and least at the poles. Phase errors due to Earth rotation can be compensated using deterministic approaches.

Phase errors are also caused by targets moving on the Earth's surface. This is especially true in the case of an ever-vibrant ocean surface. The target motion can be resolved into an along-track component and a cross-track component. A steady target velocity component U_R in the range direction produces four possible effects known as *azimuth image shift*, *azimuth image smear*, *range walk*, and *amplitude reduction*. If U_R is constant, the quadratic phase history of the return signal is not affected. However, the time at which zero Doppler is encountered is changed relative to the stationary target (facet) case.

As a consequence, the SAR processor expects stationary facets and therefore erroneously allocates the azimuth position x of the moving facet to the image position x^1 given by $x^1 = (x + \Delta x)$, where Δx is the azimuth image shift. If the direction of U_R is toward the radar, the location of the moving target is shifted in the +ve azimuth direction (i.e., in the direction of motion of the radar platform). Similarly, a target moving away from the radar in the range direction appears to be shifted in the negative

azimuth direction. For an airborne SAR for which the ground speed V may be considered the same as the radar platform speed, the shift Δx is given by (Robinson, 1985) $\Delta x = -(R/V)U_R$, and for a satellite with ground speed V and radar platform speed V_p , the shift Δx is given by (Robinson, 1985) $\Delta x = -\left(\frac{R \times V_p}{V^2}\right)U_R$, where R is the slant range. It can be seen that the facet displacement is independent of radar transmission wavelength and integration time.

For azimuth image shift to be negligible, the magnitude of Δx must be much less than the azimuth resolution W_a .

This means that U_R must be less than $\frac{V^2 \times W_a}{R \times V_p}$. An interesting example of azimuthal image shift in an oceanographic context is the ship displacement from its wake. A ship with velocity that has a component in the range direction appears to be shifted to one side of the wake. In fact, such displacement has been utilized to calculate the velocity of a ship (Vesecky and Stewart, 1982).

If the facet undergoes acceleration in a slant-range direction, a processor that is tuned for stationary facets is mismatched for this particular facet. The result is a spreading of the image in the azimuthal direction, known in the SAR literature as *azimuthal image smear*. This makes the outline of the image obscure—an effect similar to defocusing in photography. According to Alpers (1983), for a given slant range and a given radar platform velocity, the azimuthal image smear depends linearly on $a_r \tau$, where a_r is the facet acceleration in the slant-range direction and τ is the coherent single-look integration time. Accordingly, if there is no component of the facet acceleration in the slant-range direction, there will be no azimuthal image smear. Alper's reasoning for the defocusing effect has been contradicted by Ouchi (1983), who argued that if the reference signal of the SAR processor is matched to a stationary point target, then the images of the moving facets are always defocused irrespective of their propagation direction. He further argued that defocusing cannot be due to the acceleration in the slant-range direction, nor can it be because of the change in the relative radar platform velocity. Defocusing can, however, be compensated by introducing a focal adjustment parameter to the reference signal of the SAR processor.

If the target velocity component U_R in the range direction is sufficiently large to cause the target to pass through one or more range-resolution cells within the time taken for the radar beam to pass over it (i.e., within the time the target is contributing to aperture synthesis), a phenomenon known as “range walk” occurs. The result of range walk is smearing in range as well as azimuth directions.

Another drawback that is characteristic of SAR systems is *speckle*. SAR speckle is the grainy, granular, noisy

phenomenon that is observed in SAR images. This is considered noise because the limit between two different homogeneous regions is faded. This noise results from interference between signals from random scatterers on a randomly moving sea surface. A mathematical treatment of SAR speckle has been given by Barber (1983). Speckle is a natural consequence of all coherent imaging systems. Speckle in radar images is often likened to the noise in images of a rough surface illuminated with laser light (Elachi, 1988). The speckle in optical images is a result of interference of the coherent light reflected by different neighboring points. It degrades the quality of the imagery. In SAR, however, speckle seems more of a nuisance than in optical images.

Speckle is characterized by a standard deviation that is as large as its average value. When viewed, the image seems dominated by multiplicative noise. The presence of speckle in SAR images reduces detectability of facets in the images as well as reducing the capability to separate and classify distributed targets. Elimination of speckle is, therefore, necessary for reliable detection of features in an image. Reduction of speckle in SAR imagery needs to be performed in such a way that the features to be detected are retained or enhanced while the random noise is removed or reduced.

The most frequently used technique for speckle reduction is “multi-look” processing, in which the synthetic aperture length is divided into N sections. The sections are synthesized separately and then averaged incoherently. In practice, multi-looks are obtained by partitioning the available signal bandwidth and processing each look independently. The final image is produced by adding the looks incoherently, pixel by pixel. In effect, several images of the same scene are produced from different sets of data in the same pass. These N images are then added to produce a single image in which the speckle noise is reduced by a factor of \sqrt{N} . The SAR images resulting from independent looks of the same scene are truly independent, because the phase fluctuations that cause the speckle change rapidly with time and look angle and so give totally different results when viewed from different parts of the synthetic aperture. A drawback of multi-look processing is that the azimuth resolution is degraded by a factor N , where N is the number of looks used for processing.

Several algorithms have been developed in the last few decades to smooth speckles for retaining edge sharpness and subtle details. Moreira (1990) reported an improved algorithm for efficient multi-look processing. This technique, however, requires approximately 50% more computational time than the traditional multi-look approach.

Image enhancement by multi-look processing is just one aspect. Developments in polarimetric SAR created another dimension toward reduction of speckle, thereby increasing the interpretability of SAR images. Polarimetric SAR data

with four elements (HH, HV, VH, and VV) of the scattering matrix make it possible to reduce the speckle effect by utilizing the correlations among co-polarized (HH, VV) and cross-polarized (HV, VH) images (Lee et al., 1990). The four elements have the following meanings:

HH = horizontal transmit, horizontal polarization received

VV = vertical transmit, vertical polarization received

HV = horizontal transmit, vertical polarization received

VH = vertical transmit, horizontal polarization received

The ideal situation is that the speckle statistics of these four terms are statistically uncorrelated, whereas the underlying reflectance is totally correlated. It is becoming common for SAR images to have multiple bands corresponding to different incident angles, different polarizations, and different frequencies, or a combination of these. Numerous filters have been designed for speckle reduction. These are based on various models for speckle, including multiplicative noise and non-Gaussian statistics. However, the image bands were filtered separately and independently. The correlation between bands was not utilized. Some recent methods of speckle filtering have been reported by Quelle et al. (1990), Nasr et al. (1990), and Samadani and Vesecky (1990).

5.4.2.4. Interferometric SAR (InSAR) System

Interferometric Synthetic Aperture Radar (InSAR) obtains images of sea surface motion signatures based on spatial contrast of sea surface roughness manifested as spatial variations in sea surface topography. InSARs can be operated from aircraft or satellite. Due to their comparably low flight velocity, airborne SARs with their single-pass capability are useful for ocean current monitoring by along-track interferometry (ATI). Airborne ATI has been used successfully to measure ocean currents (Bao et al., 1997; Carande, 1994; Goldstein et al., 1989; Goldstein and Zebker, 1987).

InSAR is a technique whereby at least two SAR images acquired with a nearly identical incidence angle (one usually regarded as master and the other slave) are combined to produce a phase interference image called an *interferogram* (Dixon, 1994; Massonnet, 1997; Zebker and Goldstein, 1986). SAR images consist of both magnitude (brightness) and phase values. If the phase information is retained, the SAR image is described as being complex (Henderson and Lewis, 1998). The phase in a complex SAR image is a coherent signal containing information about the distance between a resolution cell on the ground and the radar antenna, as well as information about the texture of terrain within a resolution cell. Using the phase information in the interferogram, it is possible to extract topographic height information using digital elevation models (DEM), height change information, and fine-scale temporal change

measurements (Burgmann et al., 2000; Okeke, 2005). Thus, InSAR exploits the phase differences of at least two complex-valued SAR images acquired from different orbit positions and/or at different times. The time gap between two passes of satellite may not be kept large, because there may be some changes in the scene that lead to temporal decorrelation. The information derived from these interferometric datasets can be used to measure several geophysical quantities, such as roughness, topography, deformations (e.g., ice fields), and ocean currents.

During the past few years, a multitude of scientific applications of InSAR techniques have evolved, and DEMs are successfully used in topographic mapping. It has been shown that InSAR is an established technique for generating high-quality DEMs from space-borne and airborne data and that it has advantages over other methods for the generation of large-area DEMs.

Processing of InSAR data is still a challenging task. For each selected image pair, several processing steps have to be performed. One of the current challenges of the InSAR application is to bring the techniques to a level where DEM generation can be executed on an operational basis. Classical InSAR processing is known to be computationally laborious (Marinkovic et al., 2004). The amount of data to be handled is enormous, the input data often expensive, the data quality *a priori* unknown, and the algorithms require fast computers. For each selected image pair, several pre-processing steps (co-registration, interferogram generation, and so on) have to be performed. A typical scene of ERS data, for instance, occupies about 650 Mbytes of computer storage. Furthermore, the quality requirements for these pre-processing steps are generally high. These call for well-articulated processing steps and organizational workflow similar to that in photogrammetry and optical remote sensing and to the level where, for instance, InSAR topographic maps are generated on an operational basis.

Okeke (2006) has described InSAR operational steps and processing chains for DEM generation from single-look complex (SLC) SAR data. The operational steps are performed in three major stages: data search, data processing, and product validation. The data processing stage is further subdivided into five steps: data pre-processing, co-registration, interferogram generation, phase unwrapping, and geocoding. Delft Object-Oriented Interferometric Software (DORIS) InSAR processing software is an efficient tool for processing of InSAR data (Kampes and Usai, 1999; Kampes et al., 2003; Kampes, 2005a). DORIS is chosen because it is fully functional interferometric processing software in the public domain. DORIS follows the classic Unix philosophy that each tool should perform a single, well-defined function, and complex functions should be built by connecting a series of simple tools into a pipeline. DORIS consists of a series of programs (modules) that perform different interferometric tasks.

5.5. ADVANCES IN THE DEVELOPMENT OF SAR TECHNOLOGY

SAR flown on the Seasat-A satellite was the first imaging radar system dedicated to imaging the ocean surface. The main objective of the Seasat-A SAR was to detect ocean waves. This system operated at 1.275 GHz (23 cm wavelength) at HH polarization at an incidence angle of $23 \pm 3^\circ$ across the swath. The choice of wavelength was based on the imagery obtained from aircraft-borne SAR systems during 1972–1974. The Seasat-A SAR system was turned on in an 800 km altitude orbit in July 1978 and gathered images until the spacecraft failed in orbit in October 1978. The imagery it gathered had a resolution of $25 \text{ m} \times 25 \text{ m}$ for four looks over a swath of 100 km width, centered about 300 km to the right of the spacecraft's ground track. The SAR's limited memory capacity and high data rate limited its operation to times when it was in view of a few ground stations equipped with dedicated SAR signal receivers.

Subsequent to the failure of Seasat-A, two SAR systems, developed by the NASA Jet Propulsion Laboratory, were flown on the space shuttle *Challenger*. The first in this series was the Shuttle Imaging Radar (SIR) known as SIR-A, launched in 1981; the second was SIR-B, launched in 1984. The imaging radars used in these missions operated in the L-band at a frequency of 1.25 GHz with HH polarization. The SAR systems in these missions achieved resolution in the range 20–40 m and swath width in the range 30–50 km. The explosion of the *Challenger*, killing everybody on board, rendered the planned SIR-C and SIR-D missions for the years 1990 and 1991 impossible.

The imaging radar experiments on the Seasat satellite and on the space shuttle *Challenger* resulted in wide interest in the use of space-borne imaging radars. The radar sensors provided unique and complementary all-weather information on sea surface dynamic phenomena similar to what was acquired with visible and infrared imagers.

Following U.S. efforts in the field of developing and launching SAR systems for surveillance of ocean surface dynamic phenomena, the U.S.S.R. launched its Almaz satellite-borne SAR in January 1991. This satellite flew at an altitude of 300 km. The SAR transmitted 9.6 cm wavelength signal at a pulse length of 33.4 s and a PRF of 3,000 Hz at HH polarization at an incident angle of $33 \pm 3^\circ$ across the swath of 40 km width, achieving sea surface resolution of $30 \text{ m (range)} \times 15 \text{ m (azimuth)}$ for single look. The Almaz SAR demonstrated its ability to generate excellent images of the sea surface features.

Based on a strong conviction among oceanographers and marine engineers about the importance of obtaining long-term data on sea surface currents and waves, a sophisticated SAR system was deployed on board the first European Remote Sensing Satellite, ERS-1, flown in July

1991. Measurements leading to the understanding of ocean circulation are one of the wide ranges of primary environmental problems addressed by the ERS-1 mission, the main thrust of which is oceanographic studies.

SAR was the major payload element of the ERS-1. A major challenge in the design of its antenna was to achieve a reasonable compromise among the requirements toward maximum system performance, the constraints imposed by the in-orbit and launcher environments, and the resulting mechanical complexity. High gain, very narrow beam width in the azimuth, and light weight are the special features of the ERS-1 SAR. The first two features necessitated the use of a long, narrow antenna. To achieve low losses, good beam-shaping capability, and good mechanical compactness, a slotted waveguide antenna concept was selected over the conventional microstrip principle. Unlike conventional designs, the antenna was made considerably light in weight, employing a novel design in which all the waveguides in the resonant array of the antenna were made from metallized carbon fiber-reinforced plastics (CFRP). The manufacturing technology for the CFRP waveguides was developed in a dedicated pre-development program that ran over the course of several years. The antenna consisted of a $10\text{ m} \times 1\text{ m}$ planar array. To permit trouble-free launching, the complete antenna was divided into 10 electrical subarrays of $1\text{ m} \times 1\text{ m}$. Every two subarrays were combined into one mechanical panel.

The SAR on ERS-1 operates in two modes: image mode and wave mode. Of these, the one useful for imaging circulation patterns is image mode. In this mode, the SAR onboard ERS-1 obtains high-resolution (30 m) imagery 100 km in width to the right of the satellite track. Its number of looks is 8. This SAR operates at a frequency of 5.3 GHz (C-band) with a bandwidth of 8.5 MHz and VV polarization and an incidence angle of 23° at midswath in normal operation.

Another, more sophisticated SAR is the Canadian Radarsat, with a repeat cycle of 16 days. Its unique quality permits the antenna beam to be steered electronically through a 20° to 45° angle of incidence over a 500 km track swath. Onboard, state-of-the-art tape recorders store Radarsat data, permitting worldwide information to be obtained. Sea ice and iceberg conditions detected by its SAR are transmitted from Radarsat to the ice information center at Mission Control in Ottawa, Canada. After processing, the ice information is relayed via communication satellites to ships in Arctic waters and to drilling rigs off the east coast of Canada.

There are two agencies operating SAR satellites in the civilian sector, the Canadian Space Agency (CSA) and the European Space Agency (ESA). CSA has had one SAR satellite, RADARSAT-1, in orbit since 1996. ESA launched its third SAR satellite, ENVISAT, in 2002. Its predecessors, ERS-1 and ERS-2, collected SAR images from 1992 to

2000 and from 1995 onward, respectively. Both CSA and ESA satellites have collected a large database of archival SAR images. In addition, the National Space Development Agency of Japan (NASDA) operated a SAR satellite from 1993–1998. The SAR images collected by this satellite are also available. Subsequent missions include Canadian RADARSAT 2 (C-Band), Japan ALOS (L-Band), and German TerraSAR (X-Band).

5.5.1. Interpretation of Image Data

Four important pattern elements used in human interpretation of image data are spectral, textural, contextual, and temporal features. *Spectral* features describe the overall band-to-band tonal variations in a multiband image set. *Texture* is defined as the frequency of tonal change within a given limited area. *Contextual* features contain information about the relative arrangement of large segments belonging to different categories; and *temporal* features describe changes in image attributes as a function of time.

When the range of tones in an area of interest is comparable to the range of tones in the entire range, human interpretation draws heavily on textural appearance. SAR imagery of sea ice is a good example of this phenomenon. Texture is an important spatial characteristic that is useful for identifying features or regions of interest in an image. Speckle reduction is just one aspect of SAR image enhancement. Texture enhancement is an equally significant aspect in SAR image processing. Retrieval of texture information from images buried in noise is usually performed using various kinds of digital signal processing techniques known as *texture analysis*.

In texture analysis, the most important task is to extract texture features that can then be used for the description or classification of different texture images using any one of a multitude of pattern-recognition techniques. Despite its clear-cut semantic meaning, texture is a rather vaguely defined concept. For this reason, various analysts have used different concepts for texture analysis.

Texture is an important aspect in image analysis because it involves a measure of both the spectral and spatial variations in the scene. The primitive of the image texture is a collection of pixels that share a common property and are geometrically connected. These pixels are related to the texture with a relationship that may be structural, probabilistic, or both. The properties of image texture can be described as fineness, coarseness, randomness, and regularity. Probably the most successful texture discrimination techniques are based on a spatial-statistical approach in which pixels in a selected neighborhood having special spatial relations are chosen as the data samples. A variety of numerical measures are then employed to extract the useful information necessary for differentiation. Some statistical approaches to texture

analysis may be found in [Haralick \(1979\)](#) and [Rignot and Kwok \(1990\)](#).

In a texture segmentation procedure, texture discrimination techniques are used to separate and identify regions of different textures in images. The most commonly used method is to classify each pixel individually. Pixel classification requires a determination of the texture in the pixel's immediate neighborhood. The size of the neighborhood window chosen to process the texture features has to be large enough to provide a statistically meaningful sample. A faster computational approach to texture segmentation has been provided by [Du \(1990\)](#) based on localized spatial filtering. In this approach, filters are chosen for each class with parameters to match its frequency, bandwidth, and spatial orientation. Segmentation is then accomplished by designating each pixel as belonging to the class with the filter that produced the strongest response at that location. It is a process whereby image regions of different textures are separated by sensing the localized changes of spatial frequency and its orientation. Texture analysis is a topic unto itself, and a discussion on this aspect is beyond the scope of this work.

5.6. DETECTION OF SEAWATER CIRCULATION FEATURES USING RAR AND SAR

Aircraft- and satellite-borne real and synthetic aperture imaging radar systems are widely used to obtain a description of sea surface manifestations of ocean circulation features in two ways. One method is imaging circulation features such as large-scale oceanic convections, eddies, fronts, Langmuir circulation, tidal currents, water flow over shallow topography, and surf zone circulation cells by measuring sea surface roughness signatures of these phenomena. The other method obtains a quantitative description of polar circulation through monitoring ice movements.

In the case of phenomena such as short-lived drifting eddies, a large part of the oceanographic, commercial, and naval interest is simply locating the circulation trajectory and its features rather than quantifying the flow vectors. The success of microwave imaging radar detection of mesoscale circulation features depends on several factors, such as enhanced wave breaking at the Bragg scale, slope and refraction changes of the dominant surface gravity waves, wind discontinuity, direct interaction of Bragg waves with currents, redistribution of surfactant materials (e.g., as in the presence of Langmuir circulation), and atmospheric instability as related to sea surface temperature variations. A single mechanism does not generally dominate the observed roughness signature but rather depends on a diverse set of oceanographic and meteorological conditions.

Microwave imaging radars respond only to surface phenomena. However, these phenomena are often indicative of ocean internal dynamics, such as subsurface eddies and internal waves. The surface expressions of these internal dynamics become visible in active microwave radar images, primarily due to the modulation of backscattering cross-section strength caused by the interaction of these dynamic phenomena with Bragg-resonant sea surface waves and the resulting redistribution of short sea-wave patterns. In such a situation, the visibility of the feature is not so much a general image intensity enhancement but rather an organized pattern of small features ([Vesecky et al., 1982](#)).

Ocean fronts (i.e., regions of current shear at the interface of different water masses) are also ocean features of great interest that can be observed from active microwave imaging radars. Because gradients often exist in a large current velocity field, the motion of microwave scatterers within the flow velocity field exhibit local perturbations and therefore express local sea surface roughness differences. These differences appear as variations in image brightness. Thus, shear patterns associated with the boundary of intense current systems as well as striations associated with local variations in the flow velocity field may also be seen in the radar images. [Lyzenga \(1998\)](#) has reported SAR images of ocean fronts and internal waves.

[Johannessen et al. \(1990\)](#) have reported imaging of a variety of mesoscale sea surface roughness patterns by airborne synthetic aperture radar. These surface roughness patterns depicted a variety of surface expressions of upper-ocean circulation features such as current shear, offshore meandering jet, surface slicks with spiraling structure, long wave-current refraction, and internal waves. Comparison with "ground truth" data has shown ([Johannessen et al., 1990](#)) that the SAR frontal expression is characterized by a narrow, bright line of increased backscatter with equal darker zones of less intense backscatter on both sides.

Ocean fronts are potentially observable in radar images due to a change in surface roughness and a corresponding change in radar backscatter across the front. Changes in sea surface roughness can be caused by interaction of surface waves, with the current shear and convergence associated with the front, or damping of short waves by surfactant materials accumulated along the front. These surface roughness changes cause corresponding variations in radar backscatter due to Bragg scattering, as modified by the tilting effects of longer waves and possibly due to other mechanisms associated with small-scale wave breaking. The thin linear features often observed in the SAR images of intense current shear regions would correspond to the local saturation of SAR resonant waves as they interact with the current shear. These filamentary structures probably correspond both to the local saturation

taking place as resonant waves reach their maximum penetration into the current and to the shear itself tending to transform an initially compact region of high backscattering cross-section into multiple linear features (Vesecky et al., 1982).

Surprisingly, the SAR system could also reveal warm-water rings, although it is essentially a roughness-sensing device. It is believed that the mechanism of detection of thermal signatures in some fronts is the change in the short gravity wave field related to wind-stress changes across the front, which is a result of differences in boundary layer stability on each side of the thermal gradient associated with the front. The ring is marked by a series of straight and curved filamentary structures ~ 1 km in width and as long as 150 km in length. It is believed that these filamentary features are generated due to current shear within the eddy. These rings are often likened to a midsection slice through an onion. The SAR image inside a ring is generally brighter and has a mottling distinct from the surrounding water mass. During the Norwegian Continental Shelf Experiment, simultaneous C- and X-band SAR data were examined, supported by *in situ* measurements, using a ship-mounted acoustic Doppler current profiler, a CTD, and cup anemometers, and detected a complicated mesoscale circulation pattern associated with meander growth, eddy formation, and intrusion of Atlantic water toward the Norwegian coast. SAR features imaged due to ocean circulation patterns such as current shears, frequently present along ocean fronts and eddies, cause narrow backscatter changes that appear as bright lines.

In addition to the open-ocean phenomena just discussed, SAR systems can also image tidal flows and other features of coastal inlets. When tidal currents and their gradients are large, the SAR resonant waves interacting with the current variations enhance the relative backscattering cross-section, thereby providing a bright image. Another mechanism that enhances the SAR image intensity is the steepening of long gravity waves (i.e., waves with a wavelength much larger than the resonant wavelength) by interaction with tidal currents. These tilted waves would then enhance the radar return as they become steeper. At shallow depths, tidal current parallel streaks, supposed to be responsible for the formation of longitudinal tidal bedforms such as sand ribbons and erosional furrows, have also been detected using SAR images (Kenyon, 1983). Detection of current parallel streaks not only helps explain the formation of longitudinal bedforms but also gives a more accurate measurement of the direction of current flow.

Another circulation phenomenon often observed in SAR images is the internal wave-induced surface current. Surface manifestations of internal waves apparently arise because the currents associated with these waves modify the capillary-ultragravity wave spectrum overlying the oscillations. However, the exact mechanisms producing the

modifications are not fully understood. The radar resonant sea waves can interact strongly with the internal waves if the internal and surface waves are traveling in the same direction and the group velocity (C_g) of the surface waves is near resonant with the phase velocity (C_i) of the internal waves. In shallow water, internal wave amplitudes can be large and the induced surface current velocities also quite large. In such a situation, significant modulation of radar resonant waves can occur over a wider range of $(C_i - C_g)$, and radar detection of the resulting scattering cross-section modulation is more likely. Probably this is the reason that internal wave features are so frequently seen in SAR imagery of continental shelf waters.

Another interesting circulation phenomenon that can clearly be seen on radar images is the wind-driven Langmuir circulations associated with helical roll vortices. Debris such as surface films or floating seaweeds trapped in the Langmuir circulation cell regions modulate the radar return, thereby causing image contrast enhancement. Surface films concentrated along the convergence regions of these cells damp the local resonant waves and therefore reduce radar image intensity. In current-divergence regions the dispersal of surface films would cause the energy density of resonant surface waves to be larger than that in the adjacent regions, thereby permitting enhancement of image contrast.

Strong estuarine tidal currents and surf zone circulation are yet other classes of circulation phenomena that are detectable in active microwave radar images. Tidal currents in estuaries often possess strong current gradient at certain phases of the tide. At these phases the Bragg resonant waves are strongly refracted and strained. Such modulations cause increased roughness contrast. Breaking of the shoaling waves is vigorous in the high-velocity regions of the surf zone. Because these high-velocity regions have strong backscattering cross-sections, one must expect that these regions will be seen as brighter in the radar image. On the contrary, longshore and rip-current regions in the image are darker compared to the neighboring areas. This “blacking out” in the SAR image occurs when the orbital velocities of the shoaling waves are of the order of their phase velocity (Alpers et al., 1981). In this case, the azimuthal displacement of the moving facets can become so large that they are shifted completely out of the image if the azimuthal bandwidth of the radar is limited. It is surprising that image suppression arising from fast-moving targets, which is an inherent defect of the SAR imaging process, has become a useful feature for detecting circulation patterns in the surf zone that generally has a bright background because of strong backscattering cross-section of the breaking waves.

There have been instances where the incursion of the Gulf Stream onto the shelf injected multiple water masses on the continental shelf near Cape Hatteras, North

Carolina; these were accompanied by surface-intensified fronts with strong surface shear and convergence (Marmorino and Trump, 1994). A glimpse into the frontal and water mass structure occurring in this region has been provided by microwave imaging radars (Marmorino et al., 1998). The X-band radar measurements used in this study were collected at horizontal polarization and at near-grazing angles. This type of measurement has been shown to be particularly sensitive to wave breaking and to have a large dynamic range across ocean signatures such as fronts and slicks (Askari et al., 1996; Trizna and Carlson, 1996). The observed radar frontal signatures are about a factor of 30 above background levels. Radar image of a 2- by 5-km area of the sea surface showed narrow bands of high radar backscatter (indicating locally rough water) intersecting in the shape of a narrow wedge connecting to a single band and thus having the appearance of a *Y*. Similar radar features appear in the works by Fu and Holt (1982), Hayes (1981), Graber et al. (1996), and Lyzenga (1998) and so are not uncommon on this part of the shelf.

Marmorino et al. (1998) proposed that features like these represent intersecting ocean fronts, which become visible in the imagery through the refraction and steepening of surface waves by across-front current convergence and shear. According to them, a *Y* forms because the relatively buoyant water behind one front will always overwash the water ahead of it, erasing that part of the frontal expression from the surface. Such a configuration can be likened to an atmospheric occluded front. The frontal structure was revealed in the ship's radar imagery as well as in airborne radar imagery. The width of a frontal radar signature provides an approximate estimate of the width of the velocity front because the increase in surface roughness measured by the radar is associated with both the local surface velocity gradients and the integrated velocity change across the front (e.g., Lyzenga, 1991). The widths of the frontal signatures are in the range of 50–75 m.

5.7. MEASUREMENT OF SEA SURFACE CURRENTS USING IMAGING OF ICE FLOES

With the advent of satellite-borne microwave imaging technology, continuous mapping of the motion of a large number of ice floes simultaneously has become possible. The Canadian Radarsat's SAR frequently covers the entire Arctic region, regardless of weather or darkness. Within a few hours of the satellite's passage overhead, the processed SAR image can be made available to a rig or ship.

As already noted, two techniques are currently in use for detection of icebergs using active microwave imaging

technology: detection of "sidelighted character" and roughness contrast. Whereas the former method was used for the last few decades, the latter method could be operationalized only with the advent of multipolarized SAR and advanced texture analysis techniques. When the signature arising from the sidelighted character of ice floes is utilized, salinity differences of the iceberg and the surrounding seawater play no role in the imaging process. For this reason, newborn icebergs that have electrical properties that are the same as those of the surrounding water, as well as refrozen aged icebergs that have reduced salt content and, therefore, have electrical properties that are different from those of the surrounding water, can be detected by a microwave radar with the same efficiency, provided that the icebergs are large enough to protrude well above the sea surface to appear as a topographic relief.

The sidelighted character of topographic relief arises through local variations in the slope of the relief, which result in varying angles of signal incidence. This, in turn, results in relatively stronger backscatter from slopes facing the radar and weak or no backscatter from areas blocked from sufficient illumination by the radar wave. The "radar shadows" from these areas will appear in the imagery as completely black and sharply defined, unlike shadows in photography that are weakly illuminated by energy scattered by the atmosphere. The oblique illumination of the side-looking aircraft-borne microwave radar produces strong backscattered returns from the side of a large iceberg-facing antenna, in comparison to the returns from the surrounding seawater surface. The portion of the iceberg that obstructs the radar beam creates a shadow. The radar illumination becomes more oblique in the far-range direction, and therefore the shadows are proportionately longer. The contrast between the highlighted and the shadow regions of the iceberg makes the image more pronounced in the far-range direction.

The potential of microwave radar systems to observe iceberg movement and, therefore, water current circulation in the polar regions is very promising. Leberl (1979) utilized repetitive aircraft-borne synthetic aperture radar coverage of a test site in the Arctic region to measure the regional sea ice drift. *Ice drift* is the change of position of individual ice features over time. Drift is measured by comparing sequential maps of the distribution of a selected set of ice features. To extract quantitative information on ice drift from microwave radar imagery, individual image strips are usually *rectified*. In radar imaging terminology, image rectification is a process by which image measurements are transformed into geographical coordinates. Rectification requires accurate radar platform navigation data. In the study conducted by Leberl (1979) in the Arctic, radar images were taken at different seasons through clouds and fog and, in some cases, during the night. This study demonstrated that the all-time, all-weather capability

makes microwave radar a remote-sensing tool well suited to providing data on sea ice movement.

A major problem with iceberg monitoring has been the difficulty in distinguishing between icebergs and ships. Large icebergs may be distinguished from ships because of the differences in their shapes. With smaller ones, distinction purely on the basis of imagery of the target is rather difficult. There is, however, an ingenious mechanism that permits the image interpreter to distinguish between icebergs moving under the influence of advection. The several waves generated by a moving ship form a V-shaped Kelvin wake behind the ship. These waves may be classified into three general categories: (1) surface waves generated by the ship, (2) vortex wakes, and (3) internal waves generated by the ship. Theoretically, the angle that the limiting shape of this Kelvin wake subtends in deep water is approximately 39° . Vesecky et al. (1982) reported ship wakes, as imaged by Seasat SAR, of lengths varying from a few kilometers to approximately 20 km and limiting angles varying from 18° to 23° . The overall V-shaped envelope of the wake shows up as a region of greater surface roughness relative to the fairly smooth region outside this envelope. Some attempts have recently been made to understand the mechanism of backscatter modulations within the ship wake field. The present view is that the vortices shed by the ship give rise to a current at the surface. This current interacts with the ocean surface waves, thereby causing backscatter modulations.

The advent of satellite-borne SARs has brought considerable interest in the use of microwave imagery to study movement of arctic ice floes. A common approach to the automated tracking of arctic ice had been to select a patch of ice floes from an early image (the source image) and to cross-correlate it with a later image (the target image) at each position that could plausibly correspond to the same patch of ice. The position that maximizes the computed correlation coefficient is deemed likely to contain the corresponding patch of ice. Sometimes consistency checks between several matches are used to identify false matches. This method is known as *area correlation*. A disadvantage of this method is its computational expense, especially in cases where ice floes rotate. To accommodate rotation, the patch must be rotated and correlated several times at each potential match position in the target image. The search space thus becomes very large, thereby increasing enormously the computational burden. As a result, there has been increasing attention to algorithms for tracking ice floes by matching feature shapes. Rather than correlating raw pixel values, these algorithms first extract features from the images. The shapes of the extracted features are then compared using shape descriptors. One method of tracking ice floes using shape comparison is based on normalized correlation. The

second method is based on *dynamic time warping*. These methods effectively tackle rotation of ice floes.

The ERS-1 satellite, launched in July 1991, was a good tool for surveillance of sea-ice motion. Maps of ice motion and ice type will be routinely produced at the Alaska SAR facility using radar imagery. Detection, classification, and motion analysis of thin ice floes in open water bodies became reality with the development of advanced texture analysis techniques and ice-motion algorithms. The use of texture analysis considerably improved the contrast between ice and open water. An experienced image interpreter can distinguish textures corresponding to different types of targets.

REFERENCES

- Ahmed, S., Warren, H.R., Symonds, D., Cox, R.P., 1990. The Radarsat system. *IEEE Trans. Geosci. Remote Sens.* 28, 598–602.
- Alpers, W., 1983. Imaging ocean surface waves by synthetic aperture radar: A review. In: Allen, T.D. (Ed.), *Satellite microwave remote sensing*. Ellis Horwood Limited, Chichester, England, pp. 107–119.
- Alpers, W.R., Ross, D.B., Rufenach, C.L., 1981. On the detectability of ocean surface waves by real and synthetic aperture radar. *J. Geophys. Res.* 86 (C7), 6481–6498.
- Askari, F., Donato, T.F., Morrison, J.M., 1996. Detection of oceanic fronts at low grazing angles using an X-band real aperture radar. *J. Geophys. Res.* 101, 20,883–20,898.
- Austin, R.W., 1979. Coastal Zone Colour Scanner radiometry. *SPIE*, 208—*Ocean Optics*, 170–177.
- Bamler, R., Eineder, M., 1996. ScanSAR processing using standard high precision SAR algorithms. *IEEE Trans. Geosci. Remote Sens.* 34, 212–218.
- Bamler, R., Hartl, P., 1998. Synthetic aperture radar interferometry. *Inverse Problems* 14, R1–R54.
- Bao, M., Bruning, C., Alpers, W., 1997. Simulation of ocean waves imaging by along-track interferometric synthetic aperture radar. *IEEE Trans. Geosci. Remote Sens.* 35, 618–631.
- Barber, B.C., 1983. Some properties of SAR speckle. In: Allen, T.D. (Ed.), *Satellite microwave remote sensing*. Ellis Horwood Limited, Chichester, West Sussex, England, pp. 129–145.
- Blume, H.C., Love, A.W., Van Melle, M.J., Ho, W.W., 1977. Radiometer observations of sea temperature at 2.65 GHz over the Chesapeake Bay. *IEEE J. Oceanic Eng.* OE-2 (1), 121–128.
- Burgmann, R., Rosen, P.A., Fielding, E.J., 2000. Synthetic Aperture Radar interferometry to measure Earth's surface topography and its deformation. *Annual Review Earth Planetic Sciences* 28, 169–209.
- Calla, O.P., 1984. Microwave sensors (present and future). In: Deekshatulu, B.L., Rajan, Y.S. (Eds.), *Remote Sensing*. Indian Academy of Science, pp. 15–25.
- Carande, R.E., 1994. Estimating ocean coherence time using dual-baseline interferometric synthetic aperture radar. *IEEE Trans. Geosci. Remote Sens.* 32, 846–854.
- Caraux, D., Austin, R.W., 1983. Delineation of seasonal changes of chlorophyll frontal boundaries in Mediterranean coastal waters with

- Nimbus-7 Coastal Zone Colour Scanner data. *Remote Sensing of Environment* 13, 239–249.
- Carrara, W.G., Goodman, R.S., Majewski, R.M., 1995. *Spotlight synthetic aperture radar: Signal processing algorithms*. Artech House, Boston, MA, USA.
- Clarke, G.L., Ewing, G.C., Lorenzen, C.J., 1970. Spectra of backscattered light from the sea obtained from aircraft as a measure of chlorophyll concentration. *Science* 167, 1119–1121.
- Cumming, I.G., Guo, Y., Wong, F., 1997. A comparison of phase-preserving algorithms for burst-mode SAR data processing. *Int. Geoscience and Remote Sensing Symp. IGARSS '97*, 731–733. (Singapore).
- Di Cenzo, A., 1988. Strip mode processing of spotlight synthetic aperture radar data. *IEEE Trans. Aerosp. Electron. Syst.* 24, 225–230.
- Dixon, T.H., 1994. SAR interferometry and surface change detection. Report of Workshop. Boulder, Colorado, USA.
- Du, L.J., 1990. Texture segmentation of SAR images using localized spatial filtering. *Proc. 10th Annual International Geoscience & Remote Sensing Symposium* vol. III, 1983–1986.
- Elachi, C., 1980. Space-borne imaging radars: Geologic and oceanographic applications. *Science* 209, 1073–1082.
- Elachi, C., 1988. *Space-borne radar remote sensing: Applications and techniques*. IEEE, New York, NY, USA.
- Francis, C.R., Thomas, D.B., Windsor, E.P.L., 1983. The evaluation of SMMR retrieval algorithms. In: Allan, T.D. (Ed.), *Satellite Microwave Remote Sensing*. Ellis Horwood Limited, Chichester, England, pp. 481–498.
- Fu, L.-L., Holt, B., 1982. Seasat views oceans and sea ice with synthetic aperture radar. *JPL Publ.*, 81–120.
- Gagliardini, D.A., Karszenbaum, H., 1984. Application of Landsat MSS, NOAA/TIROS AVHRR, and Nimbus CZCS to study the La Plata River and its interaction with the ocean. *Remote Sensing of Environment* 15, 21–36.
- Gerson, D., Khedouri, E., Gaborski, P., 1982. Detecting the Gulf Stream from digital infrared data pattern recognition. In: *Processes in Marine Remote Sensing*, pp. 19–39.
- Gloersen, P., Barath, F.T., 1977. A scanning multichannel microwave radiometer for Nimbus-G and Seasat-A. *IEEE J. Oceanic Eng.* OE-2 (2), 172–178.
- Goldstein, R.M., Zebker, H.A., 1987. Interferometric radar measurement of ocean surface current. *Nature* 328, 707–709.
- Goldstein, R.M., Barnett, T.P., Zebker, H.A., 1989. Remote sensing of ocean current. *Science* 246, 1282–1285.
- Gordon, H.R., Clark, D.K., Mueller, J.L., Hovis, W.A., 1980. Phytoplankton pigments from the Nimbus-7 Coastal Zone Colour Scanner: Comparisons with surface measurements. *Science* 210, 63–66.
- Gordon, H.R., Clark, D.K., Brown, J.W., Brown, O.B., Evans, R.H., 1982. Satellite measurement of the phytoplankton pigment concentration in the surface waters of a warm core Gulf Stream ring. *J. Marine Res.* 40 (2), 491–502.
- Gordon, H.R., Mueller, J.L., Wrigley, R.C., 1980. Atmospheric correction of Nimbus-7 Coastal Zone Colour Scanner imagery. In: Deepak, A. (Ed.), *Remote Sensing of Atmospheres and Oceans*. Academic Press, New York, NY, USA, pp. 457–483.
- Gough, P.T., Hawkins, D.W., 1997. Unified framework for modern synthetic aperture imaging algorithms. *Int. J. Imaging Syst. Technol.* 8, 343–358.
- Graber, H.C., Thompson, D.R., Carande, R.E., 1996. Ocean surface features and currents measured with SAR interferometry and HF radar. *J. Geophys. Res.* 101, 25,831–25,832.
- Haralick, R.M., 1979. Statistical and structural approaches to texture. *Proc. IEEE* 67, 786–804.
- Harris, T.F.W., Legeckis, R., Forest, D.V., 1978. Satellite infrared images in the Agulhas Current System. *Deep-Sea Res.* 25, 543–548.
- Hayes, R.M., 1981. Detection of the Gulf Stream. In: Beal, R.C., DeLeonibus, P.S., Katz, I. (Eds.), *Spaceborne synthetic aperture radar for oceanography*, Johns Hopkins Oceanogr. Stud. 7. Johns Hopkins University Press, Baltimore, MD, USA.
- Henderson, F.M., Lewis, A.J. (Eds.), 1998. *Principles and Application of Imaging Radar, Manual of Remote Sensing*, 2. Wiley, New York, NY, USA.
- Hillger, D.W., Haar, T.H.V., 1988. Estimating noise levels of remotely sensed measurements from satellite using spatial structure analysis. *J. Atmos. Oceanic Technol.* 5, 206–214.
- Holligan, P.M., Aarup, T., Groom, S.B., 1989. The North Sea: Satellite Colour Atlas. *Cont. Shelf Res.* 9 (8), 667–765.
- Hovis, W.A., Clark, D.K., Anderson, F., Austin, R.W., Wilson, W.H., Baker, E.T., Ball, D., Gordon, H.R., Mueller, J.L., El-Sayed, S.Z., Sturm, B., Wrigley, R.C., Yentsch, C.S., 1980. Nimbus-7 Coastal Zone Colour Scanner: System description and initial imagery. *Science* 210 (4465), 60–63.
- Inman, D., Tait, R., Nordstrom, C., 1971. Mixing in the surf zone. *J. Geophys. Res.* 76, 3493–3514.
- Irvine, D.E., Tilley, D.G., 1988. Ocean wave directional spectra and wave-current interaction in the Agulhas from the Shuttle Imaging Radar-B synthetic aperture radar. *J. Geophys. Res.* 93 (C12), 15,389–15,401.
- Johannessen, J.A., Shuchman, R.A., Johannessen, O.M., 1990. NORSEX '88: A pre-launch ERS-1 satellite study of SAR imaging capabilities of upper ocean circulation features and wind fronts. *Proc. 10th Annual International Geoscience & Remote Sensing Symposium* vol. 1, 707–710.
- Jordan, R.L., 1980. The SEASAT-A synthetic aperture radar system. *IEEE J. Oceanic Eng.* OE-5 (2), 154–164.
- Kampes, B.M., 2005a. *Delft Object-oriented Interferometric Software (DORIS)*. Delft, the Netherlands, Bert Kampes, TU.
- Kampes, B.M., Usai, S., 1999. DORIS: The Delft Object-oriented Radar Interferometric Software. 2nd International Symposium on Operationalization of Remote Sensing, Enschede, the Netherlands.
- Kampes, B.M., Hanssen, R.F., Perski, Z., 2003. Radar interferometry with public domain tools. *FRINGE 2003 Workshop*, ESA/ESRIN, Frascati, Italy.
- Katsaros, K., 1980. Radiative sensing of sea surface temperature. In: Dobson, F., Hasse, L., Davis, R. (Eds.), *Air-Sea Interaction, Instruments and methods*. Plenum Press, New York, pp. 293–317.
- Kenyon, N.H., 1983. Tidal current bedforms investigated by Seasat. In: Allen, T.D. (Ed.), *Satellite microwave remote sensing*. Ellis Horwood Limited, pp. 261–270.
- La Violette, P.L., Chabot, P.L., 1969. A method of eliminating cloud interference in satellite studies of sea surface temperatures. *Deep-Sea Res.* 16, 539–547.
- Leberl, F., Bryan, M.L., Elachi, C., Farr, T., Campbell, W., 1979. Mapping of sea ice and measurement of its drift using aircraft synthetic aperture radar images. *J. Geophys. Res.* 84, 1827–1835.

- Lee, J.S., Grunes, M.R., Mango, S.A., 1990. Speckle reduction in polarimetric SAR imagery. *Proc. 10th Annual International Geoscience & Remote Sensing Symposium* vol. III, 2431–2434.
- Lee, T.N., Atkinson, L.P., Legeckis, R., 1981. Observations of a Gulf Stream frontal eddy on the Georgia continental shelf, April 1977. *Deep-Sea Res.* 28A (4), 347–378.
- Legeckis, R., 1987. Satellite observations of a western boundary current in the Bay of Bengal. *J. Geophys. Res.* 92 (C1 2), 12,974–12,978.
- Li, F.K., Johnson, W.T.K., 1983. Ambiguities in space-borne synthetic aperture radar systems. *IEEE Trans. Aerosp. Electron. Syst.* AES-19, 389–397.
- Lillesand, T.M., Kiefer, R.W., 1979. *Remote Sensing and Image Interpretation*. Wiley, New York.
- Lowe, D., 1980. Acquisition of remotely sensed data. In: Siegal, B.S., Gillespie, A.R. (Eds.), *Remote sensing in geology*. Wiley, New York, pp. 47–90.
- Lyzenga, D.R., 1991. Interaction of short surface and electromagnetic waves with ocean fronts. *J. Geophys. Res.* 96, 10,765–10,772.
- Lyzenga, D.R., 1998. Effects of intermediate-scale waves on radar signatures of ocean fronts and internal waves. *J. Geophys. Res.* 103, 18,759–18,768.
- MacDonald, 1980. Techniques and applications of imaging radars. In: Siegal, B.S., Gillespie, A.R. (Eds.), *Remote sensing in geology*. Wiley, pp. 297–336.
- Marinkovic, P.S., Hanssen, R.F., Kampes, B.M., 2004. Utilization of parallelization algorithms in InSAR/PS-InSAR processing. 2004 Envisat & ERS Symposium, ESA SP-572, Salzburg, Austria.
- Marmorino, G.O., Trump, C.L., 1994. A salinity front and current rip near Cape Hatteras, North Carolina. *J. Geophys. Res.* 99, 7627–7637.
- Marmorino, G.O., Shen, C.Y., Allan, N., Askari, F., Trizna, D.B., Trump, C.L., Shay, L.K., 1998. An occluded coastal oceanic front. *J. Geophys. Res.* 103 (C10), 21,587–21,600.
- Massonnet, D., 1997. Satellite radar interferometry. *Scientific American* 276 (2), 46–53.
- Monti Guarnieri, A., Prati, C., 1996. ScanSAR focusing and interferometry. *IEEE Trans. Geosci. Remote Sens.* 34, 1029–1038.
- Monti Guarnieri, A., Prati, C., Rocca, F., 1994. Interferometry with ScanSAR. *EARSeL Newsletter*. December 20.
- Moore, R.K., Claassen, J.P., Lin, Y.H., 1981. Scanning spaceborne synthetic aperture radar with integrated radiometer. *IEEE Trans. Aerosp. Electron. Syst.* 17, 410–420.
- Moreira, A., 1990. Improved multi-look techniques applied to SAR and SCANSAR imagery. *Proc. 10th Annual International Geoscience & Remote Sensing Symposium* vol. 1, 321–324.
- Moreira, A., Mittermayer, J., Scheiber, R., 1996. Extended Chirp Scaling algorithm for air- and space-borne SAR data processing in stripmap and ScanSAR image modes. *IEEE Trans. Geosci. Remote Sens.* 34, 1123–1136.
- Munson, D.C., O'Brien, J.D., Jenkins, W.K., 1983. A tomographic formulation of spotlight-mode synthetic aperture radar. *Proc. IEEE* 71, 917–925.
- Nasr, J.M., Fernin, P., 1990. A comparison of the detection performances obtained with a fully polarized SAR and a dual polarized SAR (HH, VV). *Proc. 10th Annual International Geoscience & Remote Sensing Symposium* Vol. 1, 317–320.
- Njoku, E.G., Christensen, E.J., Cofield, R.E., 1980. The Seasat scanning multichannel microwave radiometer (SMR): Antenna pattern correction — Development and implementation. *IEEE J. Oceanic Eng.* OE-5 (2), 125–137.
- Okeke, F.I., 2005. Integrating InSAR, GRACE mission data and traditional measurements for topographic mapping and earth surface deformation monitoring for Nigeria. 1st International Conference on Geodesy and Geodynamics, Toro, Nigeria.
- Okeke, F.I., 2006. InSAR operational and processing steps for DEM generation, Promoting Land Administration and Good Governance. 5th FIG Regional Conference, Accra, Ghana. March 8–11, 2006.
- Ouchi, K., 1983. Effect of defocusing on the images of ocean waves. In: Allen, T.D. (Ed.), *Satellite microwave remote sensing*. Ellis Horwood Limited, New York, pp. 209–222.
- Philpot, W.D., Vodacek, A., 1989. Laser-induced fluorescence: Limits to the remote detection of hydrogen, ion, aluminium, and dissolved organic matter. *Remote Sensing of Environment* 29 (1), 51–65.
- Quelle, H., Boucher, J.M., 1990. Combined use of parametric spectrum estimation and Frost-Algorithm for radar speckle filtering. *Proc. 10th Annual International Geoscience & Remote Sensing Symposium* vol. 1, 295–298.
- Rignot, E., Kwok, R., 1990. Extraction of textural features in SAR images: Statistical model and sensitivity. *Proc. 10th Annual International Geoscience & Remote Sensing Symposium* vol. III, 1979–1982.
- Robinson, I.S., 1985. *Satellite oceanography: An introduction for oceanographers and remote sensing scientists*. Ellis Horwood (a division of Wiley), Chichester, England.
- Sabins Jr., F.F., 1978. *Radar imaging*. In: *Remote sensing principles and interpretation*. W. H. Freeman, New York, USA.
- Samadani, R., Vesecky, J.F., 1990. Using optimally pruned decision trees to find objects in speckled images. *Proc. 10th Annual International Geoscience & Remote Sensing Symposium* vol. III, 1975–1978.
- Shenk, W.E., Salomonson, V.V., 1972. A multispectral technique to determine sea surface temperature using Nimbus 2 data. *J. Phys. Oceanogr.* 2, 157–167.
- Smith, R.C., Baker, K.S., 1982. Oceanic chlorophyll concentrations as determined by satellite (Nimbus-7 Coastal Zone Colour Scanner). *Marine Biology* 66, 269–279.
- Smith, R.C., Brown, O.B., Hoge, F.E., Baker, K.S., Evans, R.H., Swift, R.N., Esaias, W.E., 1987. Multiplatform sampling (ship, aircraft, and satellite) of a Gulf Stream warm core ring. *Applied Optics* 26 (11), 2068–2081.
- Strong, B., Brumley, B., Terray, E.A., Kraus, N.C., 2000. Validation of the Doppler shifted dispersion relation for waves in the presence of strong tidal currents, using ADCP wave directional spectra and comparison data. *Proc. 6th Intl. Workshop on Wave Hindcasting and Forecasting*, Monterey, California, USA. November 6–10, 2000.
- Strong, B., Brumley, B., Stone, G.W., Zhang, X., 2003. The application of the Doppler shifted dispersion relationship to hurricane wave data from an ADCP directional wave gauge and co-located pressure sensor. *Proc. of the IEEE/OES Seventh Working Conference on Current Measurement Technology*, 119–124.
- Stumpf, R.P., Tyler, M.A., 1988. Satellite detection of bloom and pigment distributions in estuaries. *Remote Sensing of Environment* 24 (3), 385–404.
- Sturm, B., 1981. The atmospheric correction of remotely sensed data and the quantitative determination of suspended matter in marine water surface layers. In: Cracknell, A.P. (Ed.), *Remote sensing in meteorology, oceanography and hydrology*. Ellis Hordwood Limited, Chichester, UK, pp. 163–197.

Swanson, P.N., Riley, A.L., 1980. The Seasat scanning multichannel microwave radiometer (SMMR): Radiometric calibration algorithm development and Performance. *IEEE J. Oceanic Eng.* OE-5 (2), 116–124.

Thomas, D.P., 1981. Microwave radiometry and applications, In: *Remote Sensing in Meteorology, Oceanography and Hydrology*. In: Cracknell, A.P. (Ed.). Ellis Horwood Series in Environment Science, pp. 357–369.

Tomiyasu, K., 1974. Remote sensing of the earth by microwaves. *IEEE Proceedings* 62 (1), 86–92.

Tomiyasu, K., 1978. Tutorial review of synthetic aperture radar (SAR) with applications to imaging of the ocean surface. *IEEE Proceedings* 66 (5), 563–583.

Tomiyasu, K., 1981. Conceptual performance of a satellite borne, wide swath synthetic aperture radar. *IEEE Trans. Geosci. Remote Sens.* GE-19, 108–116.

Trizna, D.B., Carlson, D.J., 1996. Studies of dual polarized low grazing angle radar sea scatter in nearshore regions. *IEEE Trans. Geosci. Remote Sens.* 34, 747–757.

Tyler, M.A., Stumpf, R.P., 1989. Feasibility of using satellites for detection of kinetics of small phytoplankton blooms in estuaries: Tidal and migrational effects. *Remote Sensing of Environment* 27 (3), 233–250.

Ulabay, F.T., Moore, R.K., Fung, A.K., 1982. *Radar Remote Sensing and Surface Scattering and Emission Theory*, Addison-Wesley Advanced Book Program/World Science Division. Microwave Remote Sensing (Active and Passive) vol. II, 1064. Wesley publishing company, Reading, MA.

Verstappen, H.T., 1977. *Remote sensing in geomorphology*. Elsevier Scientific, Amsterdam—Oxford—New York—Tokyo.

Vesecky, J.F., Stewart, R.H., 1982. The observation of ocean surface phenomena using imagery from the SEASAT synthetic aperture radar. *J. Geophys. Res.* 87 (C5), 3397–3430.

Vigan, X., Provost, C., Podesta, G., 2000b. Sea-surface velocities from sea-surface temperature image sequences, application to the Brazil-Malvinas Confluence area. *J. Geophys. Res.* 105 (C8), 19,515–19,531.

Vigan, X., 2002. Upper-layer ocean current forecasts. *Sea Technol.* 43 (10), 15–19.

Vigan, X., Provost, C., Bleck, R., Courtier, P., 2000a. Sea-surface velocities from sea-surface temperature image sequences, method and validation using primitive equation model output. *J. Geophys. Res.* 105 (C8), 19,499–19,514.

Walker, 1980. Range-Doppler imaging of rotating objects. *IEEE Trans. Aerosp. Electron. Syst.* 16, 23–52.

Witting, J.M., 1984. Wave-current interaction: A powerful mechanism for an alteration of the waves on the sea surface by subsurface bathymetry. In: Nihoul, J.C.J. (Ed.), *Remote sensing of shelf sea hydrodynamics*. Elsevier Oceanography Series, 38. Elsevier, Amsterdam, pp. 187–203.

Yamooka, H., Kaneko, A., Park, Jae-Hun, Zheng, H., Gohda, N., Takano, T., Zhu, Xiao-Hua, Takasugi, Y., 2002. Coastal acoustic tomography system and its field application. *IEEE J. Oceanic Eng.* 27 (2), 283–295.

Yentsch, C.S., 1960. The influence of phytoplankton pigments on the colour of sea water. *Deep-Sea Res.* 7 (1), 1–9.

Zebker, H.A., Goldstein, R.M., 1986. Topographic mapping from interferometric SAR observations. *J. Geophys. Res.* 91 (B5), 4993–4999.

BIBLIOGRAPHY

Arons, A.B., Stommel, H., 1967. On the abyssal circulation of the World Ocean: III, An advection-lateral mixing model of the distribution of a tracer property in an ocean basin. *Deep-Sea Res.* 14, 441–457.

Barrick, D.E., Swift, C.T., 1980. The seasat microwave instruments in historical perspective. *IEEE J. Oceanic Eng.* OE-5 (2), 75–79.

Bogler, P.L., 1987. Motion-compensated SAR image ISLR. *IEEE Trans. Geosci. Remote Sensing* GE-25 (6), 871–878.

Born, G.H., Dunne, J.A., Lame, D.B., 1979. Seasat mission overview. *Science* 204, 1405–1406.

Brander, R., 1999. Field observations on the morphodynamic evolution of a low-energy rip current system. *Mar. Geol.* 157, 199–217.

Brown, W.J., Porcello, L., 1968. An introduction to synthetic aperture radar. *IEEE Spectrum* 6, 52–66.

Brown, O.B., Cheney, R.E., 1983. Advances in satellite oceanography: Reviews of Geophysics and Space Physics 21 (5), 1216–1230.

Davis, R., 1985. Drifter observations of coastal surface currents during code: The statistical and dynamical views. *J. Geophys. Res.* 90, 4756–4772.

Davis, R.E., 1987. Modeling eddy transport of passive tracers. *J. Mar. Res.* 45, 635–665.

Essen, H.-H., 1995. Geostrophic surface currents as derived from satellite SST images and measured by a land-based HF radar. *Int. J. Remote Sensing* 16, 239–256.

Evans, R.H., Brown, O.B., 1981. Propagation of thermal fronts in the Somali Current system. *Deep-Sea Res.* 28 A (5), 521–527.

Graber, H.C., Thompson, D.R., Carande, R.E., 1996. Ocean surface features and currents measured with synthetic aperture radar interferometry and HF radar. *J. Geophys. Res.* 101, 25,813–25,832.

Graham, L.C., 1974. Synthetic interferometer radar for topographic mapping. *Proc. IEEE* 62, 763–768.

Johannessen, O.M., Sandven, S., Jenkins, A.D., Durand, D., Pettersson, L.H., Espedal, H., Evensen, G., Hamre, T., 2000. Satellite earth observation in operational oceanography. *Coastal Eng.* 41, 155–176.

Johnson, D., Pattiaratchi, C., 2004. Transient rip currents and nearshore circulation on a swell-dominated beach. *J. Geophys. Res.* 109 (C02026).

Johannessen, J.A., Kudryavtsev, V., Akimov, D., Eldevik, T., Winther, N., Chapron, B., 2005. On radar imaging of current features: 2. Mesoscale eddy and current front detection. *J. Geophys. Res.* 110 (C07017).

Keyte, G.E., Pearson, M.J., 1983. An assessment of SEASAT-SAR image quality. In: Allen, T.D. (Ed.), *Satellite microwave remote sensing*. Ellis Horwood Limited, pp. 187–208.

Lyzenga, D.R., 1991. Interaction of short surface and electromagnetic waves with ocean fronts. *J. Geophys. Res.* 96, 10,765–10,772.

Marmorino, G.O., Thompson, D.R., Graber, H.C., Trump, C.L., 1997. Correlation of oceanographic signatures appearing in synthetic aperture radar and interferometric synthetic aperture radar imagery with in situ measurements. *J. Geophys. Res.* 102, 18,723–18,736.

McClam, P., Marks, R., Cunningham, G., McCulloch, A., 1980. Visible and infrared radiometer on Seasat-1. *IEEE J. Oceanic Eng.* OE-5 (2), 164–168.

Njoku, E.G., Stacey, J.M., Barath, F.T., 1980. The Seasat scanning multichannel microwave radiometer (SMMR): Instrument description and Performance. *IEEE J. Oceanic Eng.* OE-5 (2), 100–115.

Schwicow, R.L., 1982. Marine LiDAR for subsurface sensing. In: Vernberg, F.J., Diemer, F.P. (Eds.), *Processes in Marine Remote*

- Sensing, pp. 133–149. The Belle W. Baruch Library in Marine Science, No. 12.
- Shay, L.K., Graber, H.C., Ross, D.B., Chapman, R.D., 1995. Mesoscale ocean surface current structure detected by high-frequency radar. *J. Atmos. Oceanic Technol.* 12, 881–900.
- Strong, A.E., Derycke, R.J., 1973. Ocean current monitoring employing a new satellite sensing technique. *Science* 182 (411), 482–484.
- Sturm, B., 1981. The atmospheric correction of remotely sensed data and the quantitative determination of suspended matter in marine water surface layers. In: Cracknell, A.P. (Ed.), *Remote sensing in meteorology, oceanography, and hydrology*. Ellis Horwood Limited, Chichester, pp. 163–197.
- Teague, C.C., Tyler, G.L., Joy, J.W., Stewart, R.H., 1973. Synthetic aperture observations of directional height spectra for 7s ocean waves. *Nature* 244, 98–100.
- Teague, C.C., Ross, D., 1979. The offshore environment: A perspective from seasat-1 SAR data. *Proc. 11th annual OTC*, 215–220.
- Tomiyasu, K., 1978. Tutorial review of synthetic aperture radar (SAR) with applications to imaging of the ocean surface. *Proc. IEEE* 66 (5), 563–583.